Plexcitons: Dirac points and topological modes

Joel Yuen-Zhou[1], Semion K. Saikin[2,3], Tony H. Zhu[4,5], Mehmet C. Onbasli[6], Caroline A. Ross[6], Vladimir Bulovic[5,7], and Marc A. Baldo[5,7]
[1] *Department of Chemistry and Biochemistry, University of California San Diego, La Jolla, CA, USA.**
[2] *Department of Chemistry and Chemical Biology, Harvard University, Cambridge, MA, USA.*
[3] *Department of Physics, Kazan Federal University, Kazan 420008, Russian Federation*
[4] *Department of Physics, Massachusetts Institute of Technology, Cambridge, MA, USA.*
[5] *Center for Excitonics, Research Laboratory of Electronics, Massachusetts Institute of Technology, Cambridge, MA, USA.*
[6] *Department of Materials Science and Engineering, Massachusetts Institute of Technology, Cambridge, MA, USA. and*
[7] *Department of Electrical Engineering and Computer Science, Massachusetts Institute of Technology, Cambridge, MA, USA.*

Plexcitons are polaritonic modes that result from the strong coupling between excitons and plasmons. We consider plexcitons emerging from the interaction of excitons in an organic molecular layer with surface plasmons in a metallic film. We predict the emergence of Dirac cones in the two-dimensional bandstructure of plexcitons due to the inherent alignment of the excitonic transitions in the organic layer. These Dirac cones may open up in energy by simultaneously interfacing the metal with a magneto-optical layer and subjecting the whole system to a perpendicular magnetic field. The resulting energy gap becomes populated with topologically protected one-way modes which travel at the interface of this plexcitonic system. Our theoretical proposal suggests that plexcitons are a convenient and simple platform for the exploration of exotic phases of matter as well as of novel ways to direct energy flow at the nanoscale.

When UV-visible light is absorbed by an organic molecular aggregate, it promotes molecules from their ground to their excited electronic states. The resulting excitations, known as excitons, can migrate between molecules via a mixture of coherent and incoherent processes [1]. Understanding and controlling how this migration of energy occurs is a fundamental problem of chemistry and physics of condensed phases. Furthermore, it is also a technological problem which is relevant to the development of efficient organic solar cells and light-emitting devices as well as all-optical circuitry [2]. Many strategies to enhance the motion of excitons exist, a particularly interesting one being where they couple to surface plasmons (SPs) [3]. In such strategy, the spatial coherence of plasmons assists the transport of an exciton across lengthscales that are dozens of times larger than regular exciton diffusion lengths. When the coupling is strong, meaning that the energy exchange between the exciton and plasmon is faster than the respective decay times [5, 6, 9–11], plexcitons (a class of polaritons) emerge [9, 10], and energy can migrate ballistically over the coherence length of the plasmon. Besides their usefulness in energy transport, organic plexcitons are promised to be an exciting room-temperature "laboratory" for the study of light-matter and many-body interactions at the nanoscale [11]. In this letter, we propose novel plexcitonic phenomenona which should be readily realizable with current experimental capabilities: Dirac cones and topologically nontrivial plexcitons which travel along preferred directions at the edge of an organic layer.

Topologically nontrivial states of matter have been a topic of great interest in condensed matter physics owing to the discoveries of the Quantum Hall Effect [11], and more recently, of topological insulators [12, 13]. The systems supporting these states are characterized by topological invariants [14], integer numbers that remain unchanged by weak perturbations. Physically, a nontrivial topological invariant signals the presence of one-way edge modes that are immune against moderate amount of disorder. Even though these phenomena were first conceptualized for fermions in solids, they have been successfully generalized to bosonic systems including photons in waveguides [15–17], ring resonator arrays [18], ultracold atoms in optical lattices [19], and classical electric circuits [20, 21]. Furthermore, we have recently proposed an excitonic system consisting of a two-dimensional porphyrin film which becomes topologically nontrivial in the presence of a magnetic field [22]. A challenging feature of that proposal is the requirement of large magnetic fields (>10 T) and cryogenic temperatures to preserve exciton coherence. Even though we do not discourage the experimental implementation of the latter, we consider a conceptually different platform which, by using plexcitons, avoids the use of large magnetic fields and, under appropriate circumstances, may work at room temperature. In the last year, Dirac and topological polaritons have been proposed in other contexts, such as optomechanical arrays and inorganic materials in optical cavities. All of these works share a common goal to ours, which is the design of exotic modes in strongly coupled light-matter systems. However, there are substantial qualitative and quantitative differences arising from the choices of material (organic exciton *vs* inorganic exciton [23–25] or mechanical mode [26, 27]) and electromagnetic (SP *vs* microcavity [23–25] or photonic crystal [26, 27]) excitations. Hence, the physics involved in our plexciton system contrasts with the other proposals in terms of the energy and lengthscales involved in the excitations, the magnitude of the couplings, the genera-

* joelyuen@ucsd.edu

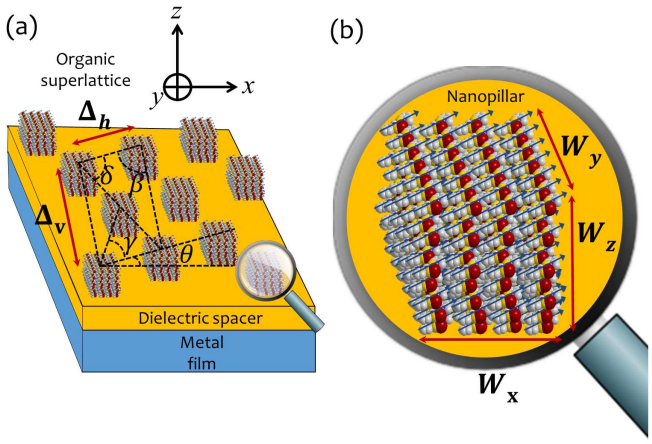

Figure 1. *Plexciton setup.* It consists of a plasmonic metal film, a dielectric spacer, and an organic layer. The latter is taken to be a monoclinic superlattice which makes an angle θ with respect to the x axis, and is further characterized by angles β,γ,δ as well as distances between nanopillars Δ_h and Δ_v. Each element in the superlattice is a nanopillar of organic emitters of dimensions W_i along each axis. When the density of emitters is big enough, the coupling between the excitons in the organic layer and the surface plasmons (SPs) in the metal becomes larger than their linewidths, giving rise to polaritonic eigenmodes that are superpositions of excitons and plasmons, or more succintly, plexcitons. In this article, we shall also consider the case where the dielectric spacer is a magneto-optical (MO) material.

tion of nontrivial topology, and the experimental conditions for its realization. Organic excitons differ from their inorganic counterparts in that they have large binding energies and are associated with large transition dipole moments. SP electromagnetic fields are strongly confined compared to their microcavity counterparts. The combination of all these properties in the organic plexciton context gives rise to strong light-matter interactions even at room temperature and in an "open cavity" setup [11].

The setup of interest is depicted in Fig. 1. It consists of three layers, from bottom to top: a plasmonic metal modelled with a Drude permittivity ($\epsilon_m(\omega)=\epsilon_\infty-\frac{\omega_P^2}{\omega^2}$, $\epsilon_\infty\sim 4$, $\omega_P\sim 9$ eV, representative parameters for Ag), an $a=10$nm thick dielectric spacer ($\epsilon_d\sim 1$), and an organic layer ($\epsilon_{org}\sim 1$). The spacer is placed to avoid quenching of the excitons by the surface plasmons (SPs) upon close contact, but as we shall see, we will also consider the case where it is a magneto-optical (MO) material.

A quantum mechanical description of this setup is given by a Hamiltonian,

$$H=H_{exc}+H_{SP}+H_{exc-SP}, \tag{1}$$

where each of the terms denotes the energetic contributions from the excitons in the organic layer, the SPs, and the coupling between them. More specifically ($\hbar=1$),

$$H_{exc}=\sum_{\boldsymbol{n},s}\omega_{\boldsymbol{n}}\sigma^\dagger_{\boldsymbol{n}}\sigma_{\boldsymbol{n}}+\sum_{\boldsymbol{n}\neq\boldsymbol{n}'}(J_{\boldsymbol{n}\boldsymbol{n}'}\sigma^\dagger_{\boldsymbol{n}}\sigma_{\boldsymbol{n}'}+\text{h.c.}), \tag{2a}$$

$$H_{SP}=\sum_{\boldsymbol{k}}\omega(\boldsymbol{k})a^\dagger_{\boldsymbol{k}}a_{\boldsymbol{k}}, \tag{2b}$$

$$H_{exc-SP}=\sum_{\boldsymbol{k},\boldsymbol{n}}\mathscr{J}_{\boldsymbol{k}\boldsymbol{n}}a_{\boldsymbol{k}}\sigma^\dagger_{\boldsymbol{n}}e^{i\boldsymbol{k}\cdot\boldsymbol{r}_{\boldsymbol{n}}}+\text{h.c.} \tag{2c}$$

Here, in order to obtain a specific shape of the exciton energy dispersion (see below), we have taken the organic layer to be an oblique superlattice of organic nanopillars. The superlattice is defined by the distances Δ_h (horizontal) and Δ_v (vertical), as well as angles β, γ, δ, and θ (Fig. 1a); the nanopillars are in turn rectangular parallelepipeds of densely packed organic chromophores (assuming a van der Waals distance between chromophores of 0.3 nm, ρ_{np} =37 chromophores/nm^3) with volume $V_{np}=W_xW_yW_z$ (Fig. 1b), obtained from growing a J-aggregate film [28, 29]. Given this preamble, $\sigma^\dagger_{\boldsymbol{n}}(\sigma_{\boldsymbol{n}})$ and $a^\dagger_{\boldsymbol{k}}(a_{\boldsymbol{k}})$ label the creation (annihilation) operators for the collective exciton at the $\boldsymbol{n}$-th nanopillar and the $\boldsymbol{k}$-th SP mode, respectively, where $\boldsymbol{n}$ and $\boldsymbol{k}$ are (two-dimensional) in-plane vectors denoting a position and a wavevector, respectively. J-aggregation of chromophores results in a collective transition dipole $\boldsymbol{\mu}_{\boldsymbol{n}}$ at an excitation energy $\omega_{\boldsymbol{n}}$, while the dispersion energy of the $\boldsymbol{k}$-th SP mode is denoted $\omega(\boldsymbol{k})$. Dipolar interactions $J_{\boldsymbol{n}\boldsymbol{n}'}$ couple the various nanopillars. The coupling between the exciton and the SP depends on the average in-plane location $\boldsymbol{r}_{\boldsymbol{n}}$ of the $\boldsymbol{n}$-th nanopillar, and is also dipolar in nature,

$$\mathscr{J}_{\boldsymbol{k}\boldsymbol{n}}=\sqrt{\frac{\omega(\boldsymbol{k})}{2\epsilon_0 SL_{\boldsymbol{k}}}}e^{-\alpha_{org0}(\boldsymbol{k})\bar{z}(\boldsymbol{k})}\boldsymbol{\mu}_{\boldsymbol{n}}\cdot\boldsymbol{E}(\boldsymbol{k}). \tag{3}$$

Here, $L_{\boldsymbol{k}}$ denotes a vertical (z-direction) mode-length of the SP which guarantees that the total energy of a SP prepared at the $\boldsymbol{k}$th mode is quantized at the energy $\omega(\boldsymbol{k})$, $\boldsymbol{E}(\boldsymbol{k})$ is an appropriately scaled electric field of the corresponding mode, and $e^{-\alpha_{org0}(\boldsymbol{k})\bar{z}(\boldsymbol{k})}$ yields a mean-field average of the interaction of the evanescent SP field (with decay constant α_{org0} in the organic layer) over the chromophores at different vertical positions of the nanopillar; it optimizes the interaction such that one may assume the nanopillar is a point-dipole located at the mean height $\bar{z}(\boldsymbol{k})$. The latter average renders the originally 3D system into an effectively 2D one. Detailed derivations of Eqs. (2) and (3) are available in the Supplementary Information (SI)-III.

Assuming perfect periodicity of the superlattice ($\omega_{\boldsymbol{n}}=\bar{\omega}$, $\boldsymbol{\mu}_{\boldsymbol{n}}=\boldsymbol{\mu}$) and only nearest and next-nearest neighbor (NN and NNN) dipolar interactions, we can re-express H_{exc} (Eq. (2a)) in terms of $\boldsymbol{k}$ modes. As explained in SI-IIIA, it is possible to approximate H_{exc} up to $O(|\boldsymbol{k}|^2)$ as arising from an *effective* simplified rectangular (rather than monoclinic) lattice aligned along the x, y axes, and with NN interactions only. This is a reasonable thing to do, as the topological effects we are interested arise at relatively long wavelengths. Within this approximation, we may construct

Fourier modes $\sigma^\dagger_{\boldsymbol{n}} = \frac{1}{\sqrt{N_x N_y}} \sum_{\boldsymbol{k}'} \sigma^\dagger_{\boldsymbol{k}'} e^{-i\boldsymbol{k}'\cdot\boldsymbol{r_n}}$ (here, N_i is the effective number of nanopillars along the i-th direction) and rewriting Eq. (1) in reciprocal space, we obtain $H = \sum_{\boldsymbol{k}} H_{\boldsymbol{k}}$,

$$H_{\boldsymbol{k}} = \underbrace{\omega_{exc,\boldsymbol{k}} \sigma^\dagger_{\boldsymbol{k}} \sigma_{\boldsymbol{k}}}_{\equiv H_{exc,\boldsymbol{k}}} + \underbrace{\omega(\boldsymbol{k}) a^\dagger_{\boldsymbol{k}} a_{\boldsymbol{k}}}_{\equiv H_{SP,\boldsymbol{k}}} + \underbrace{\left[\mathscr{J}(\boldsymbol{k}) a_{\boldsymbol{k}} \sigma^\dagger_{\boldsymbol{k}} + \text{h.c.}\right]}_{\equiv H_{exc-SP,\boldsymbol{k}}}, \quad (4)$$

where,

$$\omega_{exc,\boldsymbol{k}} = \bar{\omega}_{eff} + 2J_x \cos(k_x \Delta_x) + 2J_y \cos(k_y \Delta_y), \quad (5a)$$

$$\mathscr{J}(\boldsymbol{k}) = \sqrt{\left(\frac{N_x N_y}{S}\right)\left(\frac{\omega(\boldsymbol{k})}{2\epsilon_0 L_{\boldsymbol{k}0}}\right)} e^{-\alpha_{org0}(\boldsymbol{k})\bar{z}(\boldsymbol{k})} \boldsymbol{\mu}\cdot\boldsymbol{E}(\boldsymbol{k}), \quad (5b)$$

where J_i and Δ_i are effective NN hoppings and spacings along the i-th axis, respectively, $\bar{\omega}_{eff}$ is the effective nanopillar site energy, and we have taken $\boldsymbol{\mu}_{\boldsymbol{n}} = \boldsymbol{\mu}$ for all $\boldsymbol{n}$. Eq. (5b) denotes the $\boldsymbol{k}$-dependent coupling between a plasmonic mode and a collective exciton state throughout the organic layer. It features the interaction between nanopillars and the plasmonic mode, which is proportional to the square root of the total number of nanopillars $\sqrt{N_x N_y}$ coherently coupled to the plasmon (compare with Eq. (3)) [30–32].

For our simulation, we choose the length parameters $\Delta_h = 100$, $\Delta_v = 88$, $W_x = 7.5$, $W_y = 50$, $W_z = 70$ nm, and take $\beta = 13.1^o$ (see SI-IIIA for explanation of choice of parameters). Denoting the transition dipole $\boldsymbol{\mu} = \mu\hat{\boldsymbol{\mu}}$, we estimate $\mu = \sqrt{N_{np}} \times 10\,\text{D} = 9855\,\text{D}$, where $N_{np} = \rho_{np} V_{np}$ is the number of chromophores in the nanopillar; $\hat{\boldsymbol{\mu}}$ is the *in-plane* unit vector making an angle of $\alpha = 223^o$) with respect to $\hat{\boldsymbol{x}}$, that is, $\hat{\boldsymbol{\mu}} = \cos\alpha\hat{\boldsymbol{x}} + \sin\alpha\hat{\boldsymbol{y}}$. Choosing the simulation values for H_{exc} in Eq. (5a) to be $\Delta_x = \Delta_y = 50\,\text{nm}$, we get the effective parameters $\bar{\omega}_{eff} = 2.15\,\text{eV}$, $J_x = 362\,\text{meV}$, and $J_y = 107\,\text{meV}$. Fig. 2a shows superimposed dispersion curves for $H_{exc,\boldsymbol{k}}$ and $H_{SP,\boldsymbol{k}}$ independently (taking $H_{exc-SP} = 0$). The superlattice has been intentionally constructed to obtain $J_x, J_y > 0$ yielding a "dome"-like dispersion for $H_{exc,\boldsymbol{k}}$, *i.e.* it features a maximum at $\boldsymbol{k} = 0$, behaving as a 2D "H-aggregate" [1]. As for $H_{SP,\boldsymbol{k}}$, its dispersion has the shape of a rotationally symmetric "fountain," and is nothing more than the 2D rendering of the standard 1D textbook result [15], featuring a linear dependence of the energy at short wavevectors and a plateau at large ones, indicating excitations that are qualitatively closer to light or to charge oscillations in the metal, respectively.

Fig. 2b shows the two-plexciton-branch bandstructure arising from the diagonalization of Eq. (4). We notice that anticrossing gaps are noticeably opened in the vicinity of where the dispersion curves for $H_{exc,\boldsymbol{k}}$ and $H_{SP,\boldsymbol{k}}$ used to cross in Fig. 2a. This is a signature of exciton-SP coupling $H_{exc,SP,\boldsymbol{k}}$. Given a fixed wavevector direction, whenever these anticrossings occur, the lower-plexciton (LP) branch starts off as being mostly SP at short $\boldsymbol{k}$ values, but parametrically morphs into mostly exciton at large ones; the opposite happens with the upper-plexciton (UP) branch. However, probably the most striking feature of Fig. 2b is the appearance of two Dirac cones (see dashed circles) at critical wavevectors $\boldsymbol{k}^*$ in which anticrossings do not happen. Their onset coincides with the directions at which $\boldsymbol{k}$ is orthogonal to $\boldsymbol{\mu}$. Their physical origin is explained in Fig. 2e which, in its top panel, shows the in-plane electric field for the $\boldsymbol{k}$-th SP mode, $\boldsymbol{E}_\perp(\boldsymbol{k}) \equiv \boldsymbol{E}(\boldsymbol{k}) - \boldsymbol{E}(\boldsymbol{k})\cdot\hat{\boldsymbol{z}}\hat{\boldsymbol{z}}$ and is purely parallel to $\boldsymbol{k}$, $\boldsymbol{E}_\perp(\boldsymbol{k}) = \boldsymbol{E}_{\boldsymbol{k}}(\boldsymbol{k})$ (blue vector field). If all the dipoles in the organic layer are aligned (in-plane) along $\boldsymbol{\mu}$, their projection onto the SP electric field, which gives rise to the exciton-SP coupling (see Eq. (5b)), will wax and wane as a function of the azimuthal angle φ between the fixed dipole and the varying SP wavevector according to $\boldsymbol{\mu}\cdot\boldsymbol{E}(\boldsymbol{k}) \propto \cos\varphi$. Clearly, this projection will vanish if $\boldsymbol{k}$ happens to be orthogonal to $\boldsymbol{\mu}$, that is, at the special angles $\varphi = \frac{\pi}{2}, \frac{3\pi}{2}$, so that any degeneracy between the exciton and the SP modes will remain unlifted along these directions. From this physical picture, we can extract the two essential ingredients for the emergence of the plexciton Dirac cones. First, the dipoles need to be aligned to create an anisotropic exciton-SP coupling as a function of φ. Second, this alignment needs to be horizontal, as a vertical component of the dipole will couple to the vertical component of the electric field $\boldsymbol{E}(\boldsymbol{k})\cdot\hat{\boldsymbol{z}}\hat{\boldsymbol{z}}$, and this coupling, unlike its horizontal counterpart, does not vanish for any φ. It is important to note that neither of these requirements requires the use of the superlattice, which will be exploited for a different purpose (the engineering of topological edge modes, as explained in the next paragraph). Therefore, a standard organic molecular crystal with aligned transition dipoles lying on the horizontal xy plane will suffice. These plexciton Dirac cones which, to our knowledge, have not been reported in the past, should be easily detectable by collecting the reflected light spectra upon excitation of the plexcitonic system in a grating, Otto, or Kretschmann configurations [15], by systematically scanning across $|\boldsymbol{k}|$ and φ values. For a general $(|\boldsymbol{k}|, \varphi)$, the spectrum should consist of two dips as a function of dispersed energy, each associated with the corresponding eigenenergies of the LP and UP. Importantly, however, the two dips merge at the Dirac cones. In a standard plexciton dispersion measurement, one only scans across $|\boldsymbol{k}|$. Since we are interested in a two-dimensional dispersion, the scan must also be performed across φ.

Having elucidated the mechanism for the formation of plexciton Dirac cones, we proceed to entertain a more ambitious goal. We aim to engineer topologically protected plexcitons by opening the Dirac cones using a time-reversal symmetry breaking (TRSB) perturbation [14]. To accomplish this, we now assume that the dielectric spacer has magneto-optical (MO) properties; that is, upon application of a perpendicular magnetic field, its permittivity becomes anisotropic, $\epsilon_d \to \overleftrightarrow{\epsilon}_{MO}$,

$$\overleftrightarrow{\epsilon}_{MO} = \begin{bmatrix} \epsilon_d & ig & 0 \\ -ig & \epsilon_d & 0 \\ 0 & 0 & \epsilon_d \end{bmatrix}. \quad (6)$$

Materials associated with this dielectric tensor exhibit Faraday effect and are of great interest in the fabrication of

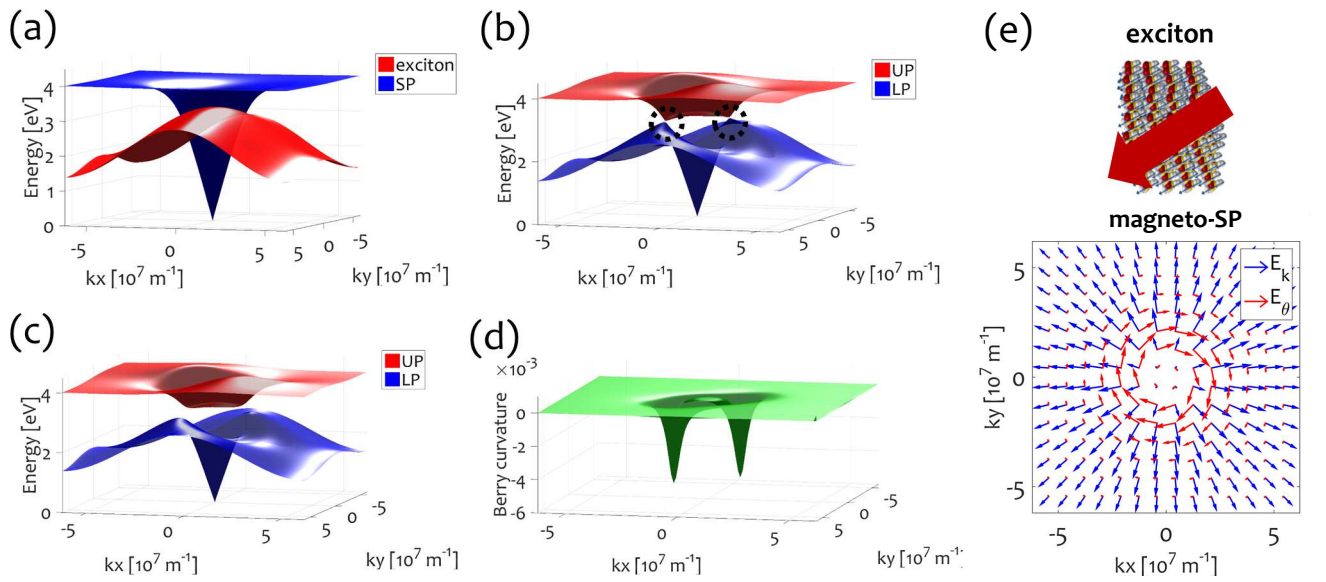

Figure 2. *Bulk plexciton properties.* Dispersion relations: (a) for SP and exciton (organic layer) modes independently, (b) when they couple in the absence of the MO effect, yielding lower (LP) and upper (UP) plexciton branches which feature two Dirac cones (dashed black circles), and (c) when they couple in the presence of the MO effect ($g = 0.3$), lifting the Dirac cones. (d) Berry curvature associated with the LP in (c). (e) Physical mechanism for the appearance of plexciton Dirac points: (top) collective (in-plane) exciton transition dipole for a nanopillar; (bottom) magnitude of the electric field of magneto-SP modes as a function of wavevector. In the absence of the MO effect, only the wavevector-parallel components $\boldsymbol{E_k}$(blue) are present. Thus, the nanopillars experience no coupling with modes whose wavevectors are perpendicular to the transition dipole. Along these directions, degeneracies between the SP and the exciton modes are not lifted, yielding two plexciton Dirac points. Nonzero tangential components $\boldsymbol{E_\theta}$ (red) emerge upon inclusion of the MO effect, lifting these degeneracies.

optical isolators [34]. For the near-IR and visible, yttrium iron garnets ($Y_3Fe_5O_{12}$, YIG) substituted with Bi (BiYIG), Ce (CeYIG) or other rare earths provide high Faraday rotation with low optical absorption [1, 2]; alternatively, one may use an MO active Co-alloy film [21] or multilayer with an insulating layer to avoid quenching of the excitons. In this article, we are interested in the new SP modes, denoted as magneto-SP modes, arising at the interface of the plasmonic metal and the MO layer. The solution for the latter is highly non-trivial, and we refer the reader to our perturbative solution in the SI-I,II, which builds a perturbation theory based upon an initial calculation due to Chiu and Quinn [13]. Fig. 2c shows essentially the same calculation as Fig. 2b, except for the inclusion of the MO effect. Interestingly, we notice that the Dirac cones have been lifted. A physical understanding of the latter phenomenon can be obtained by appealing to Fig. 2e again. Within our perturbation theory, the magneto-SP modes differ from their original SP counterparts in that there are additional tangential components (red) to the electric field. The clockwise vortex vector field is a signature of TRSB; it becomes counterclockwise upon change of direction of the magnetic field. This tangential electric field is the sole responsible for opening the Dirac cones at the critical angles $\varphi = \frac{\pi}{2}, \frac{3\pi}{2}$, where the original field (blue) ceased to couple to the excitons. Hence, we have concocted a situation where anticrossings occur for all azimuthal angles φ. To characterize the topology of the resulting bandstructure, we numerically compute the Berry curvature for each plexciton branch [39]; we show that of the LP in Fig. 2d. Its integral with respect to the Brillouin zone is the so-called Chern number C, an integer which, if nonzero, signals a topologically nontrivial phase. Fig. 2d clearly shows that this integral is non-vanishing, and in fact, adds up to $C = -1$ (by the sum rule of Chern numbers, the upper branch necessarily has $C = 1$). Intuitively, it is also clear that most of the nontrivial topology, and hence, Berry curvature, is concentrated in the vicinity of what used to be the Dirac cones. In passing, we note that considerable attention has recently been given to magneto-SPs where the magnetic field is applied parallel (instead of perpendicular) to the metal film itself, yielding dispersion relations which are nonreciprocal [40]. Curiously, this arrangement does not give us the topological states we are looking for, although it might be intriguing to explore the connection between these magneto-SPs and the ones exploited in our present work, arising from a perpendicular magnetic field.

So far, all the described calculations have been carried out in the bulk. By virtue of the bulk-boundary correspondence [14], we expect topologically protected one-way edge modes associated with this setup. In order to compute them, it is convenient to keep periodic boundary conditions for the magneto-SP modes, yet consider two domains of excitons on top (Fig. 3a), one with (in-plane) dipoles pointing along $\hat{\boldsymbol{\mu}}$ (red dipoles) and the other one with vertical dipoles along $\hat{\boldsymbol{z}}$ (blue dipoles). Pictorially, this setup resembles a "donut with two icings," where the donut is the metal with

toroidal geometry, and the two icings are the domains of excitons separated by two interfaces located at $y = \pm\frac{L_y}{2}$ and $y = 0$, where L_i is the total width of the simulated sample along i (in our calculations, we take $L_x = L_y = 6\,\mu$m). The Chern numbers associated with the bulk LP branch of each domain are $C = -1$ and $C = 0$, respectively. Hence, the plexcitons for the blue domain are topologically trivial. This can be understood by recalling that no plexciton Dirac points occur when dipoles are vertically aligned, regardless of the MO effect. In the limit of no disorder along the x-direction, k_x is still a good quantum number, and Fig. 3b shows the corresponding plexciton dispersion relation. This bandstructure is essentially a projection of the gapped 2D bulk bandstructures of both domains of plexcitons onto one axis k_x with additional states spanning the topological gap between the LP and UP branches. Inspection of the nature of these mid-gap states reveals that they have substantial exciton and magneto-SP character, and that they are precisely the edge states we are searching for: one band has positive (negative) dispersion and is localized along $y = 0$ ($y = \pm\frac{L_y}{2}$). Thus, by preparing a plexciton wavepacket localized along one of the interfaces, and making sure it is composed of energy states within this topological gap, one ensures that transport occurs robustly without much probability of backscattering. The reason being that backscattering requires coupling between counterpropagating modes which are separated by a distance $\frac{L_y}{2}$, which is large compared to the width of the corresponding wavefunctions along $\hat{\boldsymbol{y}}$. Fig. 4(a,b) shows snapshots of the dynamics associated with these edge states. Panels (a,b) and (c,d) show a plexciton that starts localized at $x = \frac{L_x}{4}$ and $x = -\frac{L_x}{4}$, respectively, and tracks the one-way (to the left or to the right) nature of their motion within the femtosecond timescale.

A useful ingredient guaranteeing the robustness of one-way transport of these edge modes is that they appear within a global gap, the latter of which is a consequence of our 2D H-aggregate superlattice design. It is easy to check that if $J_x \leq 0$ or $J_y \leq 0$, this global gap is not guaranteed anymore, and edge modes may become degenerate with bulk modes. Hence, these two types of modes could readily hybridize, yielding channels connecting one edge to the other, allowing for backscattering. Importantly however, the bandstructure remains topologically nontrivial even in the absence of such global gap, so even if perfect one-way transport is not observed in these cases, signatures of the latter may remain. Furthermore, we have shown that a superlattice with in-plane dipoles and NN and NNN couplings between nanopillars gives rise to an effective 2D H-aggregate. It is unclear whether this superlattice is necessary for our goal, or whether a simple organic molecular crystal can yield a similar behavior once we take into account all the dipolar contributions, from short to long range. These issues will be explored in future work. In the mean time, it suffices to note that, as a proof of concept, a global gap which hosts topologically protected edge states can be obtained by using an organic superlattice.

Notice that the dispersion of the edge plexcitons is such that a subset falls within the light cone ($\omega = ck_x/\sqrt{\epsilon_d}$) so far field excitation and detection of this fraction is possible via interaction with the organic layer itself. The rest of the plexcitons can be probed using the already mentioned SP measurement techniques, by launching plexcitons exciting the metallic layer itself. Furthermore, the ballistic and one-way nature of these modes can in principle be elucidated using fluorescence microscopy [41]. It is important to note that, owing to the topological nature of these states, perfect lattices are not required, so this phenomenon holds as long as orientational and site energy disorder induce perturbations which are smaller than the topological anticrossings. We tested these ideas by simulating lattices with disorder in the site energies ($\bar{\omega}_{eff} \rightarrow \bar{\omega}_{eff} + \Delta_{\bar{\omega}_{eff}}$) as well as in the orientations of the dipoles ($\hat{\boldsymbol{\mu}} \rightarrow \cos\Delta_\phi[\cos(\alpha + \Delta_\alpha)\hat{\boldsymbol{x}} + \sin(\alpha + \Delta_\alpha)\hat{\boldsymbol{y}}] + \sin\Delta_\phi\hat{\boldsymbol{z}}$), where Δ_j are chosen to be Gaussian random variables centered at 0 and having disorder widths σ_j for each $j = \bar{\omega}_{eff}, \alpha, \phi$. By systematically varying these widths independently and keeping track of the presence of the one-way edge states, we noticed that the latter survive under large amounts of disorder, whose thresholds are approximately located at $\Delta_{\bar{\omega}_{eff}} \sim 0.25\,$eV, $\Delta_\alpha \sim 30^o$, and $\Delta_\phi \sim 15^o$.

To clearly illustrate the nature of the topologically protected edge states, we have taken $\epsilon_d = 1$, $g = 0.3$, yielding a minimum gap between plexciton branches (at the wavevectors $\boldsymbol{k}^*$ of the original Dirac points) of 0.48 eV. The crossing of the SP and exciton dispersion curves happens at 3.1 eV. Given typical linewidths associated with the various dissipative mechanisms at room temperature ($\gamma_{exc,rel} \sim 5\,$meV, $\gamma_{exc,deph} \sim 40\,$meV, $\gamma_{SP,rel} \sim 10\,$meV, where rel and $deph$ stand for relaxation and dephasing), we anticipate that exciton-magneto-SP couplings need to be at least $\left|H_{exc-SP}(\boldsymbol{k}^*)\right| > \sim 10\,$meV in order for the topological plexciton edge states to be meaningful (*i.e.*, be in the regime of strong coupling [10]). Since our perturbative theory is linear in g, this means that keeping all other parameters fixed, we require $g > 0.03$. Even though this value of MO effect is very reasonable for BiYIG films, their polarizability is much larger than what we have used in our calculations; in fact, $\epsilon_d \sim 6.25$ and $g \sim 0.1$ when the perpendicular magnetic field is about 0.01 T [1], yielding $\left|H_{exc-SP}(\boldsymbol{k}^*)\right| \sim 10\,$meV, which would render the topological edge states difficult to detect, i.e., we need to reach the plexciton regime . A possible solution to this problem is to consider novel MO garnet compositions which maximize the g/ϵ_d ratio. In SI-III-4, we summarize our understanding of the optimization of $\left|H_{exc-SP}(\boldsymbol{k}^*)\right|$ for the parameter space comprised by ϵ_d, g, and a. In our simulations, we have assumed that the organic-layer has been embedded into the MO layer, since the calculation with the proper three-layer setup yielded couplings $\left|H_{exc-SP}(\boldsymbol{k}^*)\right|$ that did not surpass the dissipative linewidths. However, as far as we are aware, the weakness of the MO effect obtained with MO garnets is not fundamentally limited. Once we identify the physics that controls the strength of $\left|H_{exc-SP}(\boldsymbol{k}^*)\right|$, we can optimize the MO

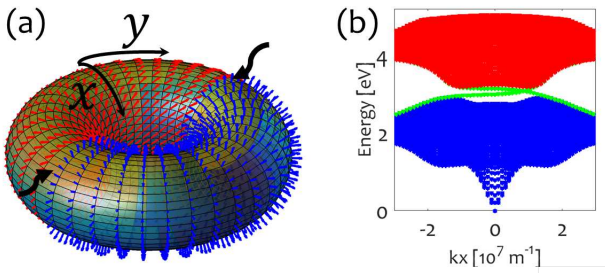

Figure 3. *Topologically protected edge modes.* (a) Simulation of edge modes where magneto-SPs are computed in the torus geometry. Two domains of organic layers are placed on top of it (just like "two icings" on a donut). In-plane (red) and out-of-plane (blue) transition dipoles yield topologically nontrivial and trivial plexcitons, respectively. Topologically protected one-way plexcitons appear at the interfaces (thick black arrows). Each interface features a different plexciton direction of motion. (b) 1D dispersion relation $\omega(k_x)$ for the setup in (a). Bulk LPs (blue) and UPs (red) separated by edge modes (green) featuring positive and negative dispersions, respectively, and localized along each interface.

layer by appealing to different engineering strategies to increase g and decrease ϵ_d (e.g. by using of MO garnet sphere arrays [42], plasmonic/magnetic metal nanostructures [21], Ce substituted YIGs [24], Eu nanocrystals [44], etc.).

In terms of the fabrication of the plexciton setup, we warn that the creation of BiYIG layers typically need high temperature and oxygen, which is incompatible with deposition on Ag or organic materials. Hence, the MO layer should first be deposited on garnet substrates such as GGG ($Gd_3Ga_5O_{12}$) (111), and subsequently floated off by dissolving or polishing the substrate. One should then transfer the film on a Ag-coated substrate and the organic layer may be deposited and patterned on garnet.

To summarize, we have described the design of exotic plexcitons via a judicious choice of material and electromagnetic excitation modes. We showed that Dirac cones and topologically protected edge states emerge from relatively simple hybrid organic/inorganic nanostructures. Even though we have not precisely identified an explicit MO material which fully satisfies our requirements, we believe its design is within reach, and is the subject of our present investigations. It is also worth noting that the physical origin of the described edges states is different from that of edge plasmons in disk geometries [45, 46], although the connections are intriguing. The possibility of directed migration of excitation energy at the nano- and mesoscale offers exciting prospects in light-harvesting and all-optical circuit architectures. Furthermore, given the recent experimental discovery of nonlinear many-body effects such as Bose-Einstein condensation of organic cavity-polaritons [47–49] and plexcitons [50] at room temperature, the introduction of the novel features described in this letter enriches the scope of these materials as a testbed for novel many-body quantum phenomena.

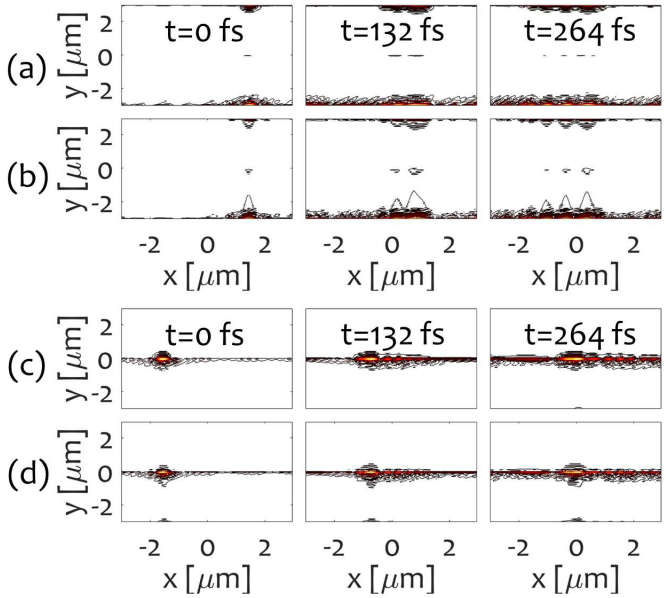

Figure 4. *Snapshots of dynamics of topologically-protected edge modes.* (a,b) and (c,d) depict the dynamics of an initially localized plexciton along the $y = 0$ and $y = \pm\frac{L_y}{2} = \pm 3\mu m$ interfaces of our smiulation. (a,c) and (b,d) show the exciton and magneto-SP components, respectively. These modes, which are robust to disorder, have substantial excitonic and magneto-SP components, travel in opposite directions along different interfaces (see Fig. 3b), and are robust against disorder.

ACKNOWLEDGEMENTS. J.Y.-Z thanks J.C.W. Song for a discussion on edge magnetoplasmons. J.Y.-Z acknowledges partial support from startup funds at UC San Diego. J.Y.-Z., T.Z., V.B., and M.B. were supported by an Energy Frontier Research Center funded by the US Department of Energy, Office of Science, Office of Basic Energy Sciences under Award Number DESC0001088. S.K.S. was supported by the Defense Threat Reduction Agency grant HDTRA1-10-1-0046. S.K.S. is also grateful to the Russian Government Program of Competitive Growth of Kazan Federal University. Finally, CAR and MCO acknowledge support of the Solid-State Solar-Thermal Energy Conversion Center (S3TEC), award DE-SC0001299, and FAME, a STARnet Center of SRC supported by DARPA and MARCO.

[1] S. K. Saikin, A. Eisfeld, S. Valleau, and A. Aspuru-Guzik. Photonics meets excitonics: natural and artificial molecular aggregates. *Nanophotonics*, 2:21–38, 2013.

[2] M. A. Baldo and V. Stojanović. Optical switching: Excitonic interconnects. *Nature Photon.*, 3(10):558–560, 2009.

[3] P. Andrew and W. L. Barnes. Energy transfer across a metal film mediated by surface plasmon polaritons. *Science*, 306(5698):1002–1005, 2004.

[4] J. Bellessa, C. Bonnand, J. C. Plenet, and J. Mugnier. Strong coupling between surface plasmons and excitons in an or-

ganic semiconductor. *Phys. Rev. Lett.*, 93:036404, 2004.

[5] A. O. Govorov, G. W. Bryant, W. Zhang, T. Skeini, J. Lee, N. A. Kotov, J. M. Slocik, and R. R. Naik. Exciton-plasmon interaction and hybrid excitons in semiconductor-metal nanoparticle assemblies. *Nano Lett.*, 6(5):984–994, 2006.

[6] A. Salomon, R. J. Gordon, Y. Prior, T. Seideman, and M. Sukharev. Strong coupling between molecular excited states and surface plasmon modes of a slit array in a thin metal film. *Phys. Rev. Lett.*, 109:073002, 2012.

[7] A. González-Tudela, P. A. Huidobro, L. Martín-Moreno, C. Tejedor, and F. J. García-Vidal. Theory of strong coupling between quantum emitters and propagating surface plasmons. *Phys. Rev. Lett.*, 110:126801, 2013.

[8] P. Törmä and W.L. Barnes. Strong coupling between surface plasmon polaritons and emitters: a review. *Rep. Prog. Phys.*, 78(1):013901, 2015.

[9] N. T. Fofang, N. K. Grady, Z. Fan, A. O. Govorov, and N. J. Halas. Plexciton dynamics: Exciton-plasmon coupling in a j-aggregate-au nanoshell complex provides a mechanism for nonlinearity. *Nano Lett.*, 11(4):1556–1560, 2011.

[10] A. Manjavacas, F. J. Garcia de Abajo, and P. Nordlander. Quantum plexcitonics: Strongly interacting plasmons and excitons. *Nano Lett.*, 11(6):2318–2323, 2011.

[11] K. v. Klitzing, G. Dorda, and M. Pepper. New method for high-accuracy determination of the fine-structure constant based on quantized hall resistance. *Phys. Rev. Lett.*, 45:494–497, 1980.

[12] C. L. Kane and E. J. Mele. Quantum spin hall effect in graphene. *Phys. Rev. Lett.*, 95:226801, 2005.

[13] B. A. Bernevig, T. L. Hughes, and S.-C. Zhang. Quantum spin hall effect and topological phase transition in hgte quantum wells. *Science*, 314(5806):1757–1761, 2006.

[14] B. A. Bernevig. *Topological Insulators and Topological Superconductors*. Princeton University Press, 2013.

[15] F. D. M. Haldane and S. Raghu. Possible realization of directional optical waveguides in photonic crystals with broken time-reversal symmetry. *Phys. Rev. Lett.*, 100:013904, 2008.

[16] A. B. Khanikaev, S. Hossein Mousavi, W. K. Tse, M. Kargarian, A. H. MacDonald, and G. Shvets. Photonic topological insulators. *Nature Mater.*, 12:233–239, 2013.

[17] L. Lu, J. D. Joannopoulos, and M. Soljačić. Topological Photonics. *ArXiv e-prints*, (8):821–829, 2014.

[18] M. Hafezi, S. Mittal, J. Fan, A. Migdall, and J. M. Taylor. Imaging topological edge states in silicon photonics. *Nature Photon.*, 7:1001–1005, 2013.

[19] M. Aidelsburger, M. Lohse, C. Schweizer, M. Atala, J. T. Barreiro, S. Nascimbene, N.R. Cooper, I. Bloch, and N. Goldman. Measuring the chern number of hofstadter bands with ultracold bosonic atoms. *Nat. Phys.*, 11(2):162–166, 2015.

[20] J. Ningyuan, C. Owens, A. Sommer, D. Schuster, and J. Simon. Time- and site-resolved dynamics in a topological circuit. *Phys. Rev. X*, 5:021031, 2015.

[21] V. V. Albert, L. I. Glazman, and L. Jiang. Topological properties of linear circuit lattices. *Phys. Rev. Lett.*, 114:173902, 2015.

[22] J. Yuen-Zhou, S. S. Saikin, N. Y. Yao, and A. Aspuru-Guzik. Topologically protected excitons in porphyrin thin films. *Nat. Materials*, 13:1026, 2014.

[23] T. Jacqmin, I. Carusotto, I. Sagnes, M. Abbarchi, D. D. Solnyshkov, G. Malpuech, E. Galopin, A. Lemaître, J. Bloch, and A. Amo. Direct observation of dirac cones and a flatband in a honeycomb lattice for polaritons. *Phys. Rev. Lett.*, 112:116402, 2014.

[24] T. Karzig, C.-E. Bardyn, N. H. Lindner, and G. Refael. Topological polaritons. *Phys. Rev. X*, 5:031001, 2015.

[25] C.-E. Bardyn, T. Karzig, G. Refael, and T.C.H. Liew. Topological polaritons and excitons in garden-variety systems. *Phys. Rev. B*, 91:161413, 2015.

[26] M. Schmidt, V. Peano, and F. Marquardt. Optomechanical Metamaterials: Dirac polaritons, Gauge fields, and Instabilities. *ArXiv e-prints*, 2013.

[27] V. Peano, C. Brendel, M. Schmidt, and F. Marquardt. Topological phases of sound and light. *ArXiv e-prints*, 2014.

[28] H. Kuhn and C. Kuhn. *J-Aggregates*, chapter Chromophore coupling effects, pages 1–40. World Scientific, 1996.

[29] M. S. Bradley, J. R. Tischler, and V. Bulovic. Layer-by-layer j-aggregate thin films with a peak absorption constant of 106 cm-1. *Adv. Mater.*, 17(15):1881–1886, 2005.

[30] F. Herrera, B. Peropadre, L. A. Pachon, S. K. Saikin, and A. Aspuru-Guzik. Quantum nonlinear optics with polar j-aggregates in microcavities. *J. Phys. Chem. Lett.*, 5(21):3708–3715, 2014.

[31] D. M. Coles, Y. Yang, Y. Wang, R. T. Grant, R. A. Taylor, S. K. Saikin, A. Aspuru-Guzik, D. G. Lidzey, J. K.-H. Tang, and J. M. Smith. Strong coupling between chlorosomes of photosynthetic bacteria and a confined optical cavity mode. *Nat. Comm.*, 5, 2014.

[32] F.C. Spano. Optical microcavities enhance the exciton coherence length and eliminate vibronic coupling in j-aggregates. *J. Chem. Phys.*, 142(18):184707, 2015.

[33] L. Novotny and B. Hecht. *Principles of Nano-Optics*. Cambridge University Press, 2012.

[34] G. F. Dionne, G.A. Allen, P.R. Haddad, C.A. Ross, and B. Lax. Circular polarization and nonreciprocal propagation in magnetic media. *Linc. Lab. J.*, 15(2):323, 2005.

[35] V. Kuzmiak, S. Eyderman, and M. Vanwolleghem. Controlling surface plasmon polaritons by a static and/or time-dependent external magnetic field. *Phys. Rev. B*, 86:045403, 2012.

[36] M.C. Onbasli, T. Goto, X. Sun, N. Huynh, and C. A. Ross. Integration of bulk-quality thin film magneto-optical cerium-doped yttrium iron garnet on silicon nitride photonic substrates. *Opt. Express*, 22(21):25183–25192, 2014.

[37] V.V. Temnov, G. Armelles, U. Woggon, D. Guzatov, A. Cebollada, A. Garcia-Martin, J.M. Garcia-Martin, T. Thomay, A. Leitenstorfer, and R. Bratschitsch. Active magneto-plasmonics in hybrid metal–ferromagnet structures. *Nat. Photon.*, 4(2):107–111, 2010.

[38] K.W. Chiu and J.J. Quinn. Magneto-plasma surface waves in solids. *Nuovo Cimento B*, 10(1):1–20, 1972.

[39] T. Fukui, Y. Hatsugai, and H. Suzuki. Chern numbers in discretized brillouin zone: Efficient method of computing (spin) hall conductances. *J. Phys. Soc. Jap.*, 74(6):1674–1677, 2005.

[40] Z. Yu, G. Veronis, Z. Wang, and S. Fan. One-way electromagnetic waveguide formed at the interface between a plasmonic metal under a static magnetic field and a photonic crystal. *Phys. Rev. Lett.*, 100:023902, 2008.

[41] G. M. Akselrod, P. B. Deotare, N. J. Thompson, J. Lee, W. A. Tisdale, M. A. Baldo, V. M. Menon, and V. Bulovic. Visualization of exciton transport in ordered and disordered molecular solids. *Nat. Commmun.*, 5, 2014.

[42] A. Christofi, N. Stefanou, and N. Papanikolaou. Periodic structures of magnetic garnet particles for strong faraday rotation enhancement. *Phys. Rev. B*, 89:214410, 2014.

[43] X. Y. Sun, Q. Du, T. Goto, M. C. Onbasli, D. H. Kim, N. M. Aimon, J. Hu, and C. A. Ross. Single-step deposition of cerium-substituted yttrium iron garnet for monolithic on-chip optical isolation. *ACS Photonics*, 2(7):856–863, 2015.

[44] Y. Hasegawa. Magnetic semiconductor euo, eus, and euse

nanocrystals for future optical devices. *Chem. Lett.*, 42(1):2–7, 2013.
[45] A. L. Fetter. Edge magnetoplasmons in a two-dimensional electron fluid confined to a half-plane. *Phys. Rev. B*, 33(6):3717, 1986.
[46] J. C. W. Song and M. S. Rudner. Chiral plasmons without magnetic field. *arXiv:1506.04743*, 2015.
[47] K.S. Daskalakis, S.A. Maier, R. Murray, and S. Kéna-Cohen. Nonlinear interactions in an organic polariton condensate. *Nat. Mater.*, 13(3):271–278, 2014.
[48] E.R. Bittner, S. Zaster, and C. Silva. Thermodynamics of exciton/polaritons in one and two dimensional organic single-crystal microcavities. *Phys. Chem. Chem. Phys.*, 14(9):3226–3233, 2012.
[49] E. R. Bittner and C. Silva. Estimating the conditions for polariton condensation in organic thin-film microcavities. *J. Chem. Phys.*, 136(3):–, 2012.
[50] S.R.K. Rodriguez, J. Feist, M.A. Verschuuren, F.J. Garcia-Vidal, and J. Gomez-Rivas. Thermalization and cooling of plasmon-exciton polaritons: Towards quantum condensation. *Phys. Rev. Lett.*, 111(16):166802, 2013.

Supplementary Information for "Plexcitons: Dirac points and topological modes"

In this Supplementary Information, we derive some results that are used in the main text of the article. We compute the electromagnetic fields associated with the magneto-surface-plasmon (magneto-SP) modes arising in two- and three-layer setups (Sec. I and Sec. II). Finally, we derive the effective 2D Hamiltonian for the plexciton system by considering the dipolar couplings between chromophores in the organic layer and between the latter and the magneto-SPs (Sec. III).

CONTENTS

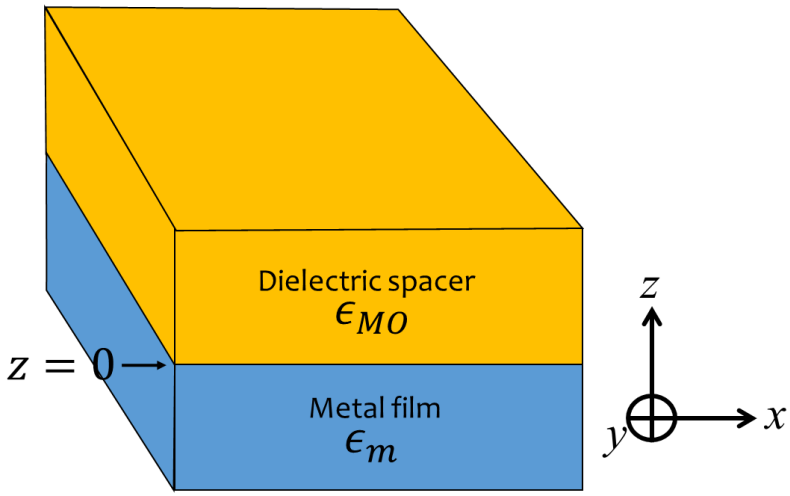

Figure S1. *Metal-MO dielectric interface at* $z = 0$. We solve for the surface plasmon (SP) modes arising at the metal-dielectric interface, in particular, when the permittivity of the dielectric $\overleftrightarrow{\epsilon}_{MO}$ is anisotropic due to the application of a perpendicular external magnetic field. The SP modes in this case are referred to as magneto-SP modes. As a first approximation to the exciton-SP coupling, we assume that the organic layer is embedded within the dielectric spacer medium.

I. MAGNETO-SPS AT A METAL-DIELECTRIC INTERFACE

A. Maxwell's equations

Maxwell's equations in arbitrary media read as follows,

$$\nabla \cdot \vec{D} = 0, \tag{S1}$$
$$\nabla \cdot \vec{B} = 0, \tag{S2}$$
$$\nabla \times \vec{E} = -\partial_t \vec{B}, \tag{S3}$$
$$\nabla \times \vec{H} = \partial_t \vec{D}. \tag{S4}$$

We are interested in the case where the electric displacement $\vec{D}$ and the magnetic field $\vec{H}$ are related to the corresponding electric fields $\vec{E}$ and the magnetic inductions $\vec{B}$ via the linear constitutive relations $\vec{D} = \epsilon_0 \overleftrightarrow{\epsilon}\vec{E}$ and $\vec{H} = \mu_0^{-1}\overleftrightarrow{\mu}^{-1}\vec{B}$, where $\epsilon_0 = 8.854 \times 10^{-12}\frac{\mathrm{C}}{\mathrm{Vm}}$ and $\mu_0 = 1.257 \times 10^{-6}\frac{\mathrm{kgm}}{\mathrm{C}^2}$ are the permittivity and permeability of vacuum, and $\overleftrightarrow{\epsilon}$ and $\overleftrightarrow{\mu}$ are the corresponding scaling (unitless) tensors for the medium in question. By taking the curl of Eq. (S3), we obtain the wave equation,

$$\nabla(\nabla \cdot \vec{E}) - \nabla^2 \vec{E} = -\frac{\overleftrightarrow{\epsilon}}{c^2}\partial_t^2 E, \tag{S5}$$

where we have introduced the free space speed of light $c = (\mu_0\epsilon_0)^{-\frac{1}{2}}$. A completely analogous equation holds for H by taking the curl of Eq. (S4), but the latter suffices for our purposes.

B. Permittivities

We are interested in (magneto-)SPs arising at the interface between a plasmonic metal (silver or gold) and a dielectric medium which is endowed with magneto-optical (MO) properties (see Fig. S1). The latter can be a mix of a magnetic oxide [1–3] dissolved in a polymer. We assume that the magnetization of both layers is null, $\overleftrightarrow{\mu} = 1$.

The permittivity of the metal is taken to be isotropic $\overleftrightarrow{\epsilon} = \epsilon_m \overleftrightarrow{I}$, where

$$\epsilon_m(\omega) = \epsilon_\infty - \frac{\omega_P^2}{\omega^2 + i\omega\gamma} \tag{S6}$$

is of the Drude form (the parameters for Ag (Au) are $\epsilon_\infty = 3.7(6.9)$, $\omega_P = 9.2(8.9)\,\text{eV}$, and $\gamma = 0.01(0.07)\,\text{eV}$ [4]). Throughout this work, we will set $\gamma = 0$ in order to keep the formalism simple. Physically, as long as the relevant energy scales of interest are larger than γ (see main text), this is a good approximation. Since we are interest in the plexciton (strong exciton-SP coupling) regime [5–11], this should be a good approximation to take. Otherwise, the quantization of the problem becomes much more complicated.

For the MO layer, the permittivity is anisotropic: upon interaction with an external magnetic field in the perpendicular z-direction, it acquires the form,

$$\overleftrightarrow{\epsilon}_{MO} = \begin{bmatrix} \epsilon_d & ig & 0 \\ -ig & \epsilon_d & 0 \\ 0 & 0 & \epsilon_d \end{bmatrix}, \tag{S7}$$

where the tensor has been written in Cartesian coordinates $(\hat{\boldsymbol{x}}, \hat{\boldsymbol{y}}, \hat{\boldsymbol{z}})$, and we take $\epsilon_d = 1$ and $g = 0.1$. Here, the off-diagonal term is proportional to the Faraday rotation that a linearly polarized plane-wave electric field experiences as it passes through the material; g changes sign upon change of magnetic field direction. Typically, MO magnetic oxides like Bismuth- and Yttrium-Iron Garnets (BIG, YIG) [1, 2] have permittivities of $\epsilon_d \sim 6$ [1–3], which imply a severe index mismatch with the metal and organic layers of interest. Hence, we are implicitly assuming that we have a Maxwell garnet blend with a low index polymer or aerogel [12] at our disposition, which yields an effective $\epsilon_d = 1$. On the other hand, $g \sim 0.1$ is a reasonable parameter for MO garnets under a magnetic field of 0.1 Tesla [1]. Just as with ϵ_m, we ignore imaginary (absorptive) contributions to ϵ_d. Subsec. III B 4 discusses other MO materials that could be used for the purposes of our study.

Chiu and Quinn [13] have solved a slightly different problem, namely, the magneto-SPs arising from a metal under a strong magnetic field coupled to a isotropic non-MO dielectric. In their study, the anisotropy arises in the metal permittivity rather than in the one corresponding to the dielectric. The resulting equations are, as expected, very similar, and one could translate their equations to our setup by some careful changes of variables. However, for clarity of presentation and in order to develop the three-layer calculation of Sec. (II), which is a generalization of the two-layer case, we shall outline the entire procedure here. Importantly, in doing so, we manage to go further than Chiu and Quinn and construct a perturbation theory in the small parameter g. This allows us to develop explicit expressions for the electromagnetic modes which, as far as we are aware, have not appeared in the literature before.

C. Electromagnetic modes for each layer

The problem is rotationally symmetric about the vertical z-direction, so it is convenient to adopt a cylindrical coordinate system. Let us search for SP modes labeled by $\boldsymbol{k}$ which propagate in-plane and decay along $\hat{\boldsymbol{z}}$ (this is precisely the condition for SP modes),

$$\vec{E}(\boldsymbol{k}) = \boldsymbol{E}(\boldsymbol{k})\, e^{i(kr_k + k_z z - \omega t)}, \tag{S8a}$$
$$\vec{B}(\boldsymbol{k}) = \boldsymbol{B}(\boldsymbol{k})\, e^{i(kr_k + k_z z - \omega t)}. \tag{S8b}$$

For a given direction of $\boldsymbol{k}$, we shall write vectors in the right-handed cylindrical coordinate system spanned by the unit vectors $\hat{\boldsymbol{k}}, \hat{\boldsymbol{\theta}}_{\boldsymbol{k}}, \hat{\boldsymbol{z}}$ such that $\hat{\boldsymbol{k}} \times \hat{\boldsymbol{\theta}}_{\boldsymbol{k}} = \hat{\boldsymbol{z}}$. for instance, $\boldsymbol{E} = (E_k, E_{\theta_k}, E_z)$, where $E_i = \boldsymbol{E} \cdot \hat{\boldsymbol{i}}$ (beware that we have defined the tangential direction of $\hat{\boldsymbol{\theta}}_{\boldsymbol{k}}$ with respect to $\hat{\boldsymbol{k}}$ and not to $\hat{\boldsymbol{r}}$). Physically, $\boldsymbol{k}$ and $\omega = \omega(\boldsymbol{k})$ denote the in-plane (propagating) wavevector and frequency of the monochromatic wave, respectively, $r_k = \boldsymbol{r} \cdot \hat{\boldsymbol{k}}$ is the projection of the position vector $\boldsymbol{r} = (r_k, r_\theta, z)$ along the $\hat{\boldsymbol{k}}$ direction, and k_z is the imaginary wavevector associated with the evanescent wave along the perpendicular direction. Inserting these modes into Eq. (S5) yields an anisotropic wave equation for $\boldsymbol{E}$,

$$\sum_{ljm} [(\delta_{il}\delta_{jm} - \delta_{im}\delta_{jl}) k_j k_l + \Omega^2 \epsilon_{im}] E_m = 0, \tag{S9}$$

where we have used the notation $\Omega(\boldsymbol{k}) = \frac{\omega(\boldsymbol{k})}{c}$ corresponding to the free space wavevector. Here, the i, j, l, m indices run through k, θ, z and, formally, we may write $\boldsymbol{k} = (k_k, k_\theta, k_z) = (k, 0, k_z)$. Due to rotational symmetry, $\overleftrightarrow{\epsilon}_{MO}$ has the same form in the $\hat{\boldsymbol{k}}, \hat{\boldsymbol{\theta}}_{\boldsymbol{k}}, \hat{\boldsymbol{z}}$ coordinates as Eq. (S7).

1. *MO layer ($z > 0$)*

Inserting the dielectric tensor associated with the MO layer (Eq. (S7)) into Eq. (S9) yields a matrix equation $\mathbb{M}_{MO}\boldsymbol{E}_{MO} = 0$ which explicitly reads as,

$$\begin{bmatrix} \epsilon_d - \Omega^{-2}k_{z,MO}^2 & ig & \Omega^{-2}kk_{z,MO} \\ -ig & \epsilon_d - \Omega^{-2}(k^2 + k_{z,MO}^2) & 0 \\ kk_{z,MO}\Omega^{-2} & 0 & \epsilon_d - \Omega^{-2}k^2 \end{bmatrix} \begin{bmatrix} 1 \\ E_{\theta,MO} \\ E_{z,MO} \end{bmatrix} = \begin{bmatrix} 0 \\ 0 \\ 0 \end{bmatrix}. \tag{S10}$$

At this point, we have chosen the arbitrary normalization condition $E_{k,MO} = 1$. The secular equation corresponding to Eq. (S10) is,

$$\left(\frac{k_z}{\Omega}\right)^4 + \mathbb{B}\left(\frac{k_z}{\Omega}\right)^2 + \mathbb{C} = 0, \tag{S11}$$

where,

$$\mathbb{B} = 2\left[\left(\frac{k}{\Omega}\right)^2 - \epsilon_d\right], \tag{S12a}$$

$$\mathbb{C} = \left[\left(\frac{k}{\Omega}\right)^2 - \epsilon_d\right]\left[\left(\frac{k}{\Omega}\right)^2 - \frac{\epsilon_d^2 - g^2}{\epsilon_d}\right]. \tag{S12b}$$

The bi-quadratic Eq. (S11) yields solutions $k_{z,MO} = i\alpha_{MO}^{\pm}, -i\alpha_{MO}^{\pm}$, where $\alpha_{MO}^{\pm}$ are two different evanescent decay or exponentially rising constants given by,

$$\alpha_{MO}^{\pm} = \Omega\sqrt{\frac{\mathbb{B}}{2} \pm \sqrt{\frac{\mathbb{B}^2}{4} - \mathbb{C}}}. \tag{S13}$$

Note that these (in general, complex-valued) constants $\alpha_{MO}^{\pm}$ must have positive real part for $e^{-\alpha_{MO}^{\pm} z}$ to decay or for $e^{\alpha_{MO}^{\pm} z}$ to rise, respectively. In the first two-layer setup we are considering, we will assume that the MO layer extends indefinitely for $z > 0$ so the field in this region must be a superposition of the two evanescent fields; exponentially rising fields will become important when we add an additional interface at $z = a$ (see Sec. II). The tangential and perpendicular components of the electric field (given $E_{k,MO} = 1$) can be obtained from Eq. (S10),

$$E_{\theta,MO}^{\pm} = \frac{-i\Omega^2 g}{k^2 - (\alpha_{MO}^{\pm})^2 - \Omega^2\epsilon_d}, \tag{S14a}$$

$$E_{z,MO}^{\pm} = \frac{ik\alpha_{MO}^{\pm}}{k^2 - \Omega^2\epsilon_d}. \tag{S14b}$$

2. *Metal layer ($z < 0$)*

In the metal, $\mathbb{M}_m \boldsymbol{E}_m = 0$ corresponds to,

$$\begin{bmatrix} \epsilon_m - \Omega^{-2}k_{z,m}^2 & 0 & \Omega^{-2}kk_{z,m} \\ 0 & \epsilon_m - \Omega^{-2}(k^2 + k_{z,m}^2) & 0 \\ kk_{z,m}\Omega^{-2} & 0 & \epsilon_m - \Omega^{-2}k^2 \end{bmatrix} \begin{bmatrix} 1 \\ E_{\theta,m} \\ E_{z,m} \end{bmatrix} = \begin{bmatrix} 0 \\ 0 \\ 0 \end{bmatrix}, \tag{S15}$$

where again we have chosen $E_{k,m} = 1$. This leads to the secular equation which yields the exponentially decaying field for $z < 0$; by letting $k_{z,m} = -i\alpha_m$,

$$\alpha_m = \sqrt{k^2 - \Omega^2\epsilon_m}. \tag{S16}$$

Eq. (S15) reveals that

$$E_{z,m} = -\frac{ik}{\alpha_m} \tag{S17}$$

but does not inform us about the tangential component $E_{\theta,m}$ as the entry $(\mathbb{M}_m)_{\theta\theta} = \epsilon_m - \Omega^{-2}(k^2 + k_{z,m}^2) = 0$. This missing component will be deduced by matching the electromagnetic fields at the boundary $z = 0$.

D. Matching the modes at the boundary ($z = 0$)

We are looking for magneto-SP modes labeled by a propagating wavevector k and frequency $\omega(\boldsymbol{k})$, but, in general, different k_z evanescent wavevectors for each layer, which we have denoted $k^{\pm}_{z,MO} = i\alpha^{\pm}_{MO}$ and $k_{z,m} = -i\alpha_m$. The energy $\omega(\boldsymbol{k})$ (and therefore Ω) is unknown.

To summarize, for each pair (k,ω), there are two possible modes in the MO layer associated with different decay constants $\alpha^{\pm}_{MO}$ (see Eq. (S13), $z>0$),

$$\begin{aligned}\vec{E}^{\pm}_{MO} &= \boldsymbol{E}^{\pm}_{MO}\eta e^{-\alpha^{\pm}_{MO}z}\\ &= (1, E^{\pm}_{\theta,MO}, E^{\pm}_{z,MO})\eta e^{-\alpha^{\pm}_{MO}z}, \qquad \text{(S18a)}\\ \vec{B}^{\pm}_{MO} &= \boldsymbol{B}^{\pm}_{MO}\eta e^{-\alpha^{\pm}_{MO}z}\\ &= \frac{-i}{\omega}(\alpha^{\pm}E^{\pm}_{\theta,MO}, -ikE^{\pm}_{z,MO} - \alpha^{\pm}_{MO}, ikE^{\pm}_{\theta,MO})\eta e^{-\alpha^{\pm}_{MO}z}, \qquad \text{(S18b)}\end{aligned}$$

where the magnetic induction in Eq. (S18b) has been deduced from Eq. (S18a) and Maxwell's Eq. (S3). The vectors have been written in cylindrical coordinates and we have defined $\eta \equiv e^{ikr-i\omega t}$. Hence, the total fields in the MO layer read,

$$\begin{aligned}\vec{E}_{MO} &= t^{+}_{MO}\vec{E}^{+}_{MO} + t^{-}_{MO}\vec{E}^{-}_{MO}, \qquad \text{(S19a)}\\ \vec{B}_{MO} &= t^{+}_{MO}\vec{B}^{+}_{MO} + t^{-}_{MO}\vec{B}^{-}_{MO}. \qquad \text{(S19b)}\end{aligned}$$

where $t^{\pm}$ are coefficients to be determined. Similarly, for the metal layer ($z<0$),

$$\begin{aligned}\vec{E}_m &= \boldsymbol{E}_m\eta e^{\alpha_m z}\\ &= (1, E_{\theta,m}, E_{z,m})\eta e^{\alpha_m z}, \qquad \text{(S20a)}\\ \vec{B}_m &= \boldsymbol{B}_m\eta e^{\alpha_m z}\\ &= \frac{-i}{\omega}(-\alpha_m E_{\theta,m}, -ikE_{z,m} + \alpha_m, ikE_{\theta,m})\eta e^{\alpha_m z}. \qquad \text{(S20b)}\end{aligned}$$

Here, we keep the arbitrary normalization where $E_{k,m} = 1$. Later on, we shall fix this normalization via quantization of the energy of the modes (see I F). Furthermore, it is also safe to arbitrarily assume $E^{\pm}_{k,MO} = 1$ because Eqs. (S19a) and (S19b) contain scaling coefficients $t^{\pm}$ which will be fixed by the boundary conditions at the metal-MO interface.

We are ready to match the fields at the interface at $z = 0$. The in-plane electric field and the perpendicular electric displacement each need to be continuous across the boundary: $E_{i,MO} = E_{i,m}$ for $i = r,\theta$, while $\epsilon_d E_{z,MO} = \epsilon_m E_{z,m}$. Furthermore, the magnetic field, and because $\overleftrightarrow{\mu} = 1$, its induction, are all continuous throughout, $B_{i,MO} = B_{i,m}$. These constraints altogether read,

$$\begin{aligned}1 &= t^{+}_{MO} + t^{-}_{MO}, \qquad \text{(S21a)}\\ E_{\theta,m} &= t^{+}_{MO}E^{+}_{\theta,MO} + t^{-}_{MO}E^{-}_{\theta,MO}, \qquad \text{(S21b)}\\ \epsilon_m E_{z,m} &= \epsilon_d(t^{+}_{MO}E^{+}_{z,MO} + t^{-}_{MO}E^{-}_{z,MO}), \qquad \text{(S21c)}\\ \alpha_m E_{\theta,m} &= -t^{+}_{MO}\alpha^{+}_{MO}E^{+}_{\theta,MO} - t^{-}_{MO}\alpha^{-}_{MO}E^{-}_{\theta,MO}, \qquad \text{(S21d)}\\ kE_{z,m} + i\alpha_m &= t^{+}_{MO}(kE^{+}_{z,MO} - i\alpha^{+}_{MO}) + t^{-}_{MO}(kE^{-}_{z,MO} - i\alpha^{-}_{MO}), \qquad \text{(S21e)}\\ E_{\theta,m} &= t^{+}_{MO}E^{+}_{\theta,MO} + t^{-}_{MO}E^{-}_{\theta,MO}. \qquad \text{(S21f)}\end{aligned}$$

These constraints read similarly to the ones derived by Chiu and Quinn in [13] (see their Eqs. (39)–(44)), except for the different coordinate conventions. Clearly, Eqs. (S21b) and (S21f) are identical. Furthermore, Eqs. (S21c) and (S21e) contain the same information, as can be shown by using Eqs. (S16) (S14b), (S17), and (S21a). The remaining constraints yield the equation,

$$\begin{aligned}&k^2 - \Omega^2\epsilon_d + \alpha^{+}_{MO}\alpha^{-}_{MO} + (\alpha^{+}_{MO} + \alpha^{-}_{MO})\alpha_m](k^2 - \Omega^2\epsilon_d)\epsilon_m\\ &+\alpha_m\epsilon_d\{\alpha^{+}_{MO}\alpha^{-}_{MO}(\alpha^{+}_{MO} + \alpha^{-}_{MO}) + \alpha_m[(\alpha^{+}_{MO})^2 + \alpha^{+}_{MO}\alpha^{-}_{MO} + (\alpha^{-}_{MO})^2] - \alpha_m(k^2 - \Omega^2\epsilon_d)\} = 0. \qquad \text{(S22)}\end{aligned}$$

By inserting Eqs. (S13), (S16) into Eq. (S22), we obtain a nonlinear equation in Ω for every value of $\boldsymbol{k}$. This equation can be numerically solved, at least in principle. Ω can be then used as input to Eqs. (S14a), (S14b), (S17), (S19a), (S19b), and (S21a)–(S21f) to solve for the electromagnetic modes. As we shall see, the most important qualitative feature of the solution of this problem is that the magneto-SP fields acquire tangential components (see Eqs. (S14a) and (S21b)) which are absent when $g = 0$ [14, 15], that is, in the absence of an external magnetic field. Eq. (S22) is identical to Eq. (45) in [13] upon carrying out the substitutions $\epsilon_{xx} = \epsilon_{zz} = \epsilon_d$.

E. Perturbation expansion on g

Chiu and Quinn reported a dispersion relation Ω *vs* $\boldsymbol{k}$ by numerically solving Eq. (S22) for a very similar setup to the one of our interest. However, a detailed description of the resulting electromagnetic modes was not presented in that work. As explained, one may in principle solve for the profile of the electromagnetic modes once this dispersion is known. However, a numerical attempt at the problem using a standard nonlinear solver yielded spurious results for the modes.

Since the solution to the SP problem with no magnetic field ($g = 0$) is a well-known textbook result, and g is anyway much smaller than ϵ_d in a realistic setup, we may use a perturbation expansion of the equation in powers of g. Our goal is to obtain the electric fields up to $O(g)$, so that we can compute the magnitude of the exciton-SP coupling to that same order. To accomplish such objective, we first need to solve for Ω as well as the coefficients $t^{\pm}_{MO}$ up to $O(g)$. As we shall see, however, knowledge of $t^{\pm}_{MO}$ requires information about Ω up to $O(g^2)$. Once this is done, we simply Taylor expand the fields (S18a), 9S18b), (S20a), (S20b) and collect the results according to Eqs. (S19a)–(S20b)). In retrospect, the original problem we faced by trying to directly solve Eq. (S22) originated from the fact that we were using the very small $O(g^2)$ corrections to Ω as an input to solve for the $O(g)$ electromagnetic modes. This requires an accurate solution of Ω, which is complicated by the highly nonlinear dependence of Eq. (S22) on Ω. As a future consideration, it might be worth exploring numerical methodologies to attack this problem beyond the perturbative regime, although for our purposes, the latter suffices.

Even though the algebra below seems involved, it is straightforward to derive using a symbolic algebra package such as Wolfram Mathematica(c).

1. *Solving for* Ω

Given that the right hand side of Eq. (S22) is zero, the polynomials at each power of g must each vanishing identically.

To start with and as a consistency check, at zeroth order in g, Eq. (S22) becomes

$$\begin{aligned}[2\alpha_{d0}^2 + 2\alpha_{d0}\alpha_{m0}]\alpha_{d0}^2\epsilon_{m0} + \alpha_{m0}\epsilon_{d0}\{\alpha_{d0}^2(2\alpha_{d0}) + \alpha_{m0}[3\alpha_{d0}^2] - \alpha_m\alpha_{d0}^2\} = \\ [2\alpha_{d0}^3 + 2\alpha_{d0}^2\alpha_{m0}](\alpha_{d0}\epsilon_{m0} + \alpha_{m0}\epsilon_{d0}) = 0,\end{aligned} \tag{S23}$$

where the 0-subscripted variables denote the corresponding functions in Eq. (S6), (S13), (S16) taking $\Omega = \Omega_0$,

$$\epsilon_{m0} = \epsilon_\infty - \frac{\Omega_P^2}{\Omega_0^2}, \tag{S24a}$$

$$\alpha_{d0} = \sqrt{k^2 - \epsilon_d\Omega_0^2}, \tag{S24b}$$

$$\alpha_{m0} = \sqrt{k^2 - \epsilon_{m0}\Omega_0^2}, \tag{S24c}$$

where $\Omega_P \equiv \frac{\omega_P}{c}$. Eq. (S23) implies that either

$$2\alpha_{d0}^3 + 2\alpha_{d0}^2\alpha_{m0} = 0, \tag{S25}$$

or

$$\alpha_{d0}\epsilon_{m0} + \alpha_{m0}\epsilon_d = 0. \tag{S26}$$

The condition in Eq. (S25) requires that $\alpha_{d0} = -\alpha_{m0}$, contradicting the very nature of the SP solution we are looking for, where α_{d0}, $\alpha_{m0} > 0$ represent evanescent fields. However, the condition in Eq. (S26) is simply the standard equation for the

dispersion relation of a SP at the interface of an unmagnetized MO sample and a metal film [14, 15]. It can be readily solved yielding,

$$k = \Omega_0 \sqrt{\frac{\epsilon_{m0}\epsilon_d}{\epsilon_{m0}+\epsilon_d}}, \tag{S27}$$

or more explicitly,

$$\Omega_0 = \sqrt{\frac{\epsilon_d\Omega_P^2 + k^2(\epsilon_d+\epsilon_\infty) - \sqrt{[\epsilon_d\Omega_P^2 + k^2(\epsilon_d+\epsilon_\infty)]^2 - 4\epsilon_\infty\epsilon_d k^2\Omega_P^2}}{2\epsilon_\infty\epsilon_d}}. \tag{S28}$$

At short k, the (linear) dispersion is very light-like, $\Omega_0 = \frac{k}{\sqrt{\epsilon_d}}$, and at large k, it plateaus to $\Omega_0 \to \frac{\Omega_P}{\sqrt{\epsilon_d+\epsilon_\infty}}$, corresponding to collective charge oscillations in the metal (see Fig. S2).

Moving on to the g^1 terms of Eq. (S22) yields an equation of the form $\Omega^{(1)} f = 0$ where $f(\alpha_{d0}, \alpha_{m0})$ is a nonzero polynomial in α_{d0} and α_{m0}, implying that $\Omega^{(1)} = 0$. This result can be quickly derived as follows: the g^1 terms stem only from the power expansion of α^+_{MO}, α^-_{MO}, α_m, and ϵ_m. Some g^1 contributions from α^+_{MO}, α^-_{MO} are proportional to Ω_1 but some are not. Regardless, the ones from α^+_{MO} come with the opposite sign to the ones from α^-_{MO}; hence, they vanish identically as Eq. (S22) is symmetric in α^+_{MO} and α^-_{MO}. On the other hand, every g^1 term for α_m and ϵ_m is strictly proportional to Ω_1 requiring $\Omega_1 = 0$ for the all the g^1 terms to cancel. Hence, the lowest order correction to Ω_0 of Ω arises at $O(g^2)$, that is,

$$\Omega \approx \Omega_0 + g^2\Omega_2. \tag{S29}$$

As mentioned, we are solely interested in the calculation of the electric fields in each layer up to $O(g)$. However, as we shall see in the next subsection, these corrections depend on Ω_2. To obtain this coefficient, we expand α^+_{MO}, α^-_{MO}, α_m, and ϵ_m up to $O(g^2)$, but not beyond that,

$$\alpha^\pm_{MO} \approx \alpha_{d0} \pm g\alpha_{d1} + g^2(\alpha_{d20} + \alpha_{d22}\Omega_2), \tag{S30a}$$
$$\alpha_m \approx \alpha_{m0} + g^2\alpha_{m22}\Omega_2, \tag{S30b}$$
$$\epsilon_m \approx \epsilon_{m0} + g^2\epsilon_{m22}\Omega_2, \tag{S30c}$$

where the coefficients in the expansions take the form,

$$\alpha_{d1} = \frac{i\Omega_0}{2\sqrt{\epsilon_d}}, \tag{S31a}$$
$$\alpha_{d20} = \frac{\Omega_0^2}{8\epsilon_d\alpha_{d0}}, \tag{S31b}$$
$$\alpha_{d22} = \frac{\Omega_0\epsilon_d}{\alpha_{d0}}, \tag{S31c}$$
$$\alpha_{m22} = -\frac{\Omega_0\epsilon_i}{\alpha_{m0}}, \tag{S31d}$$
$$\epsilon_{m22} = \frac{2\Omega_P^2}{\Omega_0^3}. \tag{S31e}$$

Notice that in order to ultimately solve for Ω_2, we have separated the g^2 terms into two categories: those which are proportional to Ω_2 ($g^2\alpha_{d22}\Omega_2$, $g^2\alpha_{m22}\Omega_2$, $g^2\epsilon_{m22}\Omega_2$) and those that are not ($g^2\alpha_{d20}$). We substitute these expressions into Eq. (S22) and collect the g^2 terms, which ought to cancel. The manipulations yield in a linear equation for Ω_2 which gives,

$$\Omega_2 = \frac{\Omega_0^5\epsilon_{m0}^2(3\epsilon_d - \epsilon_{m0})}{8\epsilon_d(\epsilon_d-\epsilon_{m0})\left[\Omega_P^2(2\alpha_{d0}^2\epsilon_{m0} + \Omega_0^2\epsilon_d^2) + \Omega_0^4\epsilon_d\epsilon_{m0}(\epsilon_d-\epsilon_{m0})\right]}, \tag{S32}$$

where we have also used Eq. (S26) in the form of $\alpha_{m0} = -\frac{\alpha_{d0}\epsilon_{m0}}{\epsilon_d}$ to simplify the final expression.

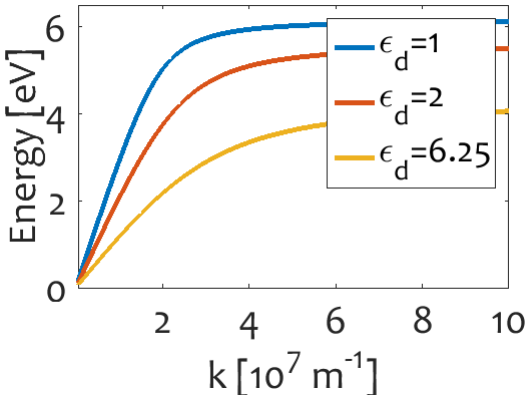

Figure S2. *SP dispersion energy as a function of* $k = |\boldsymbol{k}|$ *for the two-layer (metal-MO dielectric) setup, assuming* $g = 0$. Plots generated using Eq. (S28) with Drude parameters for Ag, $\epsilon_\infty \sim 4$, $\omega_P \sim 9$ eV, and varying the dielectric permittivity ϵ_d. Since $\Omega = \Omega_0 + O(g^2)$, the plots are correct up to $O(g)$, which is our perturbation order of interest. Notice that the dispersion curves start-off linearly (light-like excitations), but plateau to constant values at large wavevectors (charge oscillations in the metal), which become smaller as the dielectric permittivity increases.

2. *Solving for* $t^{\pm}_{MO}$

Next, we expand the coefficient t^{+}_{MO}, which denotes the contribution of the + fields in Eqs. (S19a) and (S19b) (t^{-}_{MO} can be subsequently found using the constraint in Eq. (S21a)),

$$t^{+}_{MO} \approx t_{d0} + g\, t_{d1}. \tag{S33}$$

Here, t_{d0} and t_{d1} are unknown, but we shall solve for them using the boundary condition on the perpendicular electric fields (see Eq. (S21c)). We expand $E^{\pm}_{z,MO}$ and E_{zm} in Eqs. (S14b) and (S17) up to $O(g^2)$ [1],

$$E^{\pm}_{z,MO} \approx E_{z,d0} \pm g E_{z,d1} + g^2 E_{z,d2}, \tag{S34a}$$
$$E_{z,m} \approx E_{z,m0} + g^2 E_{z,m2}, \tag{S34b}$$

where,

$$E_{z,d0} = \frac{ik}{\alpha_{d0}}, \tag{S35a}$$
$$E_{z,m0} = -\frac{ik}{\alpha_{m0}}, \tag{S35b}$$
$$E_{z,d1} = -\frac{k\Omega_0}{2\alpha^2_{d0}\sqrt{\epsilon_d}}, \tag{S35c}$$
$$E_{z,d2} = \frac{i(\alpha_{d0}\alpha_{d20}k + \alpha_{d0}\alpha_{d22}k\Omega_2 + 2k\Omega_0\Omega_2\epsilon_d)}{\alpha^3_{d0}}, \tag{S35d}$$
$$E_{z,m2} = -\frac{ik\Omega_0\Omega_2\epsilon_i}{\alpha^3_{m0}}. \tag{S35e}$$

We plug these expressions into Eq. (S21c). At zeroth-order in g, we get $\epsilon_{m0}E_{zm0} = \epsilon_d E_{zd0}$, which is equivalent to Eq. (S26) and does not give us information on t_{d0} or t_{d1} (this indeterminacy ultimately reveals why we need expansions up to $O(g^2)$

[1] Here, as opposed to Eqs. (S30a)–(S30c), we have not separated the g^2 terms in $E^{\pm}_{z,MO}$ and E_{zm} (g^2E_{zd2} and g^2E_{zm2}) into those contributions which are proportional to Ω_2 and those which are not, as Ω_2 has already been determined in Eq. (S32).

to obtain fields up to $O(g)$). At $O(g)$ we get the intuitive result,

$$t_{d0} = \frac{1}{2}, \tag{S36}$$

and at $O(g^2)$ we obtain,

$$\begin{aligned} t_{d1} &= \frac{-E_{z,d2}\epsilon_d + E_{z,m0}\Omega_2\epsilon_{m22} + E_{z,m2}\epsilon_{m0}}{2E_{zd1}\epsilon_d} \\ &= \underbrace{i\left(\frac{16\alpha_{d0}^3\alpha_{m0}^2\Omega_2\Omega_P^2 + 8\alpha_{d0}^3\Omega_0^4\Omega_2\epsilon_\infty\epsilon_{m0} + \alpha_{m0}^3\Omega_0^5 + 8\alpha_{m0}^3\Omega_0^4\Omega_2\epsilon_d^2}{8\alpha_{d0}\alpha_{m0}^3\Omega_0^4\sqrt{\epsilon_d}}\right)}_{\equiv\tau_{d1}}, \end{aligned} \tag{S37}$$

which, together with Ω_2 in Eq. (S32), can be readily evaluated with zeroth-order parameters. We notice that t_{d1} is purely imaginary-valued, so we have written it in terms of a purely real-valued τ_{d1}. Given Eq. (S33), it is clear from Eq. (S21a) that

$$t_{MO}^- \approx t_{d0} - g\,t_{d1}. \tag{S38}$$

3. *Collecting the expressions for the fields*

We now have all the ingredients to evaluate $\vec{E}_{MO}$ and $\vec{B}_{MO}$ (see Eqs. (S19a)–(S19b)) up to $O(g)$,

$$\vec{E}_{MO} \approx \vec{E}_{d0} + g\vec{E}_{d1}, \tag{S39a}$$
$$\vec{B}_{MO} \approx \vec{B}_{d0} + g\vec{B}_{d1}, \tag{S39b}$$

where, at zeroth-order, in the absence of external magnetic field, we have the standard SP mode which is a transverse magnetic (TM) mode [14, 15],

$$\vec{E}_{d0} = \underbrace{\left(1, 0, \frac{ik}{\alpha_{d0}}\right)}_{\equiv \boldsymbol{E}_{d0}}\eta_0 e^{-\alpha_{d0}z}, \tag{S40a}$$

$$\begin{aligned} \vec{B}_{d0} &= \frac{-i}{\Omega_0 c}\left(0, \frac{k^2}{\alpha_{d0}} - \alpha_{d0}, 0\right)\eta_0 e^{-\alpha_{d0}z} \\ &= \underbrace{-\frac{i\epsilon_d\Omega_0}{\alpha_{d0}c}(0,1,0)}_{\equiv \boldsymbol{B}_{d0}}\eta_0 e^{-\alpha_{d0}z}. \end{aligned} \tag{S40b}$$

In going from the first to the second line of Eq. (S40b), we have used Eq. (S24b). Eqs. (S40a)–(S40b) feature an elliptically-polarized electric field with no tangential component, and a purely tangential and imaginary-valued magnetic induction. The opposite is true for the first-order correction: it consists of a purely tangential and imaginary-valued electric field (recall that t_{d1} is purely imaginary, see Eq. (S37)) and an elliptically polarized electric field with no tangential part,

$$\vec{E}_{d1} = \underbrace{\frac{i\Omega_0(4\tau_{d1}\sqrt{\epsilon_d} - \Omega_0 z)}{2\alpha_{d0}}(0,1,0)}_{\equiv \boldsymbol{E}_{d1}}\eta_0 e^{-\alpha_{d0}z}, \tag{S41a}$$

$$\vec{B}_{d1} = \underbrace{\frac{1}{2\alpha_{d0}c}\left(-4\alpha_{d0}\tau_{d1}\sqrt{\epsilon_d} + \Omega_0(1-\alpha_{d0}z), 0, ik(4\tau_{d1}\sqrt{\epsilon_d} - \Omega_0 z)\right)}_{\equiv \boldsymbol{B}_{d1}}\eta_0 e^{-\alpha_{d0}z}. \tag{S41b}$$

In deriving Eqs. (S39a)–(S41a), we have used the $O(g)$ Taylor expansion for the fields (see Eqs. (S14a)–(S14b), (S18b)). Notice that besides the exponentially decreasing dependence of the fields, we also obtain a polynomial contribution in z.

We already computed some of the relevant expansion coefficients in Eqs. (S34a)–(S35c); the remaining ones that we used are,

$$E^{\pm}_{\theta,MO} \approx \pm\frac{\Omega_0\sqrt{\epsilon_d}}{\alpha_{d0}}, \tag{S42a}$$

$$B^{\pm}_{r,MO} \approx \mp\frac{i\sqrt{\epsilon_d}}{c} + g\frac{\Omega_0}{2\alpha_{d0}c}, \tag{S42b}$$

$$B^{\pm}_{\theta,MO} \approx -\frac{i\Omega_0\epsilon_d}{\alpha_{d0}c} + g\frac{\Omega_0^2\sqrt{\epsilon_d}}{2\alpha_{d0}^2c}, \tag{S42c}$$

$$B^{\pm}_{z,MO} \approx \pm\frac{k\sqrt{\epsilon_d}}{\alpha_{d0}c}, \tag{S42d}$$

as well as those for the plane wave components,

$$\begin{aligned}\eta e^{-\alpha^{\pm}_{MO}z} &= e^{i(kr-\omega t)-\alpha^{\pm}_{MO}z} \\ &\approx \underbrace{e^{i(kr-c\Omega_0 t)}}_{\equiv\eta_0} e^{-\alpha_{d0}z}\left(1 \mp g\frac{i\Omega_0}{2\sqrt{\epsilon_d}}z\right).\end{aligned} \tag{S43}$$

Finally, given $\vec{E}_{MO}$, $\vec{E}_m$ can be readily obtained from the boundary conditions for the fields at $z=0$ (see Eqs. (S21a)–(S21f)) as well as the original ansatz for their functional forms (see Eq. (S20a)–(S20b)),

$$\vec{E}_m \approx \vec{E}_{m0} + g\vec{E}_{m1}, \tag{S44}$$

where, at zeroth-order we have the standard SP electric field as if there were no magnetic field present,

$$\vec{E}_{m0} = \left(1, 0, \frac{\epsilon_d}{\epsilon_{m0}}\frac{ik}{\alpha_{d0}}\right)\eta_0 e^{\alpha_{m0}z} = \underbrace{\left(1, 0, -\frac{ik}{\alpha_{m0}}\right)}_{=\boldsymbol{E}_{m0}}\eta_0 e^{\alpha_{m0}z}, \tag{S45a}$$

$$\vec{B}_{m0} = \frac{i\epsilon_{m0}\Omega_0}{\alpha_{m0}c}(0,1,0)\eta_0 e^{\alpha_{m0}z} = \underbrace{-\frac{i\epsilon_d\Omega_0}{\alpha_{d0}c}(0,1,0)}_{\equiv\boldsymbol{B}_{m0}}\eta_0 e^{\alpha_{m0}z}. \tag{S45b}$$

Here, we have used Eq. (S26) in both lines. Similarly, the first order correction to $\vec{E}_{m0}$ is,

$$\vec{E}_{m1} = \underbrace{\frac{2i\tau_{d1}\Omega_0\sqrt{\epsilon_d}}{\alpha_{d0}}(0,1,0)}_{\equiv\boldsymbol{E}_{m1}}\eta_0 e^{\alpha_{m0}z}, \tag{S46}$$

$$\vec{B}_{m1} = \underbrace{\frac{2\tau_{d1}}{\alpha_{d0}c}\left(\Omega_0 - \alpha_{d0}\sqrt{\epsilon_d}, 0, ik\sqrt{\epsilon_d}\right)}_{\equiv\boldsymbol{B}_{m1}}\eta_0 e^{\alpha_{m0}z}.$$

F. Quantization and normalization of modes

The previous section shows how to (perturbatively) compute the frequency Ω, the electric field, and the magnetic induction of an SP mode with wavevector $\boldsymbol{k}$. Note that, so far, we have invoked an arbitrary normalization (setting $E_r = 1$). To fix this, we first ought to compute the energy associated with the unnormalized modes. Consider placing electric field amplitude $\mathscr{A}_{\boldsymbol{k}}$ into the radial component of the $\boldsymbol{k}$ mode. The energy in this mode is quadratic in the fields[2] [15, 16],

[2] Note that even if the electric field is much larger than the magnetic induction, the prefactors of ϵ_0 and $\frac{1}{\mu_0}$ weigh them in a way that their contributions to the energy density are on the same order of magnitude

$$H_{SP,\boldsymbol{k}} = \frac{1}{2}\sum_i \int dV \left[\epsilon_0 \sum_j \frac{d(\omega\epsilon^*_{ij}(\omega))}{d\omega}(\vec{E})^*_j(\vec{E})_i + \frac{1}{\mu_0\mu}|(\vec{B})_i|^2\right]|\mathscr{A}_{\boldsymbol{k}}|^2, \tag{S47}$$

where $i,j \in \{r,\theta,z\}$, and electric field and magnetic inductions in each $\boldsymbol{k}$ mode (throughout z) are conveniently written as,

$$\vec{E} = \Theta(-z)\vec{E}_m + \Theta(z)\vec{E}_{MO}, \tag{S48a}$$
$$\vec{B} = \Theta(-z)\vec{B}_m + \Theta(z)\vec{B}_{MO}, \tag{S48b}$$

and $(\vec{E})_i$, $(\vec{B})_i$ denote the i-th components of the respective fields (which include the plane wave exponential factors, see (S19a)–(S20b)). In Eq. (S47), we have absorbed the electric field units into $\mathscr{A}_{\boldsymbol{k}}$, so E_i is taken to be a unitless quantity. The integration $\int dV$ is carried out over all 3D space.

Assuming a finite size box of in-plane area S and infinite perpendicular dimension and plugging in Eqs. (S19a), (S19b), (S20a), and (S20b) into Eq. (S47), we obtain,

$$\begin{aligned}
H_{SP,\boldsymbol{k}} &= \frac{S|\mathscr{A}_{\boldsymbol{k}}|^2}{2}\sum_i \int_{-\infty}^{\infty} dz\Big(\epsilon_0\sum_j \frac{d(\omega\epsilon^*_{ij}(\omega))}{d\omega}(\vec{E})^*_j(\vec{E})_i + \frac{1}{\mu_0\mu}|(\vec{B})_i|^2\Big) \\
&= \frac{S|\mathscr{A}_{\boldsymbol{k}}|^2}{2}\sum_i \sum_{\gamma,\delta\in\{+,-\}} (t^{\gamma}_{MO})^* t^{\delta}_{MO}\left[\epsilon_0\sum_j \epsilon^*_{MO,ij}(E^{\gamma}_{j,MO})^* E^{\delta}_{i,MO} + \frac{1}{\mu_0\mu}(B^{\gamma}_{i,MO})^* B^{\delta}_{i,MO}\right] \\
&\qquad \times\left[\int_0^{\infty} dz e^{-[(\alpha^{\gamma}_{MO})^* + \alpha^{\delta}_{MO}]z}\right] \\
&\quad + \frac{S|\mathscr{A}_{\boldsymbol{k}}|^2}{2}\sum_i \left[\epsilon_0\frac{d(\omega\epsilon_m(\omega))}{d\omega}|E_{i,m}|^2 + \frac{1}{\mu_0\mu}|B_{i,m}|^2\right]\left[\int_{-\infty}^{0} dz e^{(\alpha^*_0+\alpha_0)z}\right] \\
&= S|\mathscr{A}_{\boldsymbol{k}}|^2\sum_i \sum_{\gamma,\delta\in\{+,-\}} (t^{\gamma}_{MO})^* t^{\delta}_{MO}\left[\epsilon_0\sum_j \epsilon^*_{MO,ij}(E^{\gamma}_{j,MO})^* E^{\delta}_{i,MO} + \frac{1}{\mu_0\mu}(B^{\gamma}_{i,MO})^* B^{\delta}_{i,MO}\right]\frac{1}{2(\alpha^*_{\gamma}+\alpha_{\delta})} \\
&\quad + S|\mathscr{A}_{\boldsymbol{k}}|^2\sum_i \left[\epsilon_0\frac{d(\omega\epsilon_m(\omega))}{d\omega}|E_{i,m}|^2 + \frac{1}{\mu_0\mu}|B_{i,m}|^2\right]\frac{1}{2(\alpha^*_m+\alpha_m)} \\
&\equiv S\left(\frac{\epsilon_0 L_{\boldsymbol{k}}}{4}\right)\left(2|\mathscr{A}_{\boldsymbol{k}}|^2\right) \\
&= S\frac{\epsilon_0 L_{\boldsymbol{k}}}{4}(\mathscr{A}_{\boldsymbol{k}}\mathscr{A}^*_{\boldsymbol{k}} + \mathscr{A}^*_{\boldsymbol{k}}\mathscr{A}_{\boldsymbol{k}}),
\end{aligned} \tag{S49}$$

where, following [16], we have defined the vertical mode length as,

$$\begin{aligned}
L_{\boldsymbol{k}} &= \sum_i \sum_{\gamma,\delta\in\{+,-\}} (t^{\gamma}_{MO})^* t^{\delta}_{MO}\left[\epsilon_0\sum_j \epsilon^*_{MO,ij}(E^{\gamma}_{j,MO})^* E^{\delta}_{i,MO} + \frac{1}{\mu_0\mu}(B^{\gamma}_{i,MO})^* B^{\delta}_{i,MO}\right]\frac{1}{\epsilon_0(\alpha^*_{\gamma}+\alpha_{\delta})} \\
&\quad + \sum_i \left[\epsilon_0\frac{d(\omega\epsilon_m(\omega))}{d\omega}|E_{i,m}|^2 + \frac{1}{\mu_0\mu}|B_{i,m}|^2\right]\frac{1}{\epsilon_0(\alpha^*_m+\alpha_m)}.
\end{aligned} \tag{S50}$$

Since E_i is taken to be unitless, $L_{\boldsymbol{k}}$ effectively has units of length. Physically, $L_{\boldsymbol{k}}$ defines a mode volume $SL_{\boldsymbol{k}}$ with a quantized amount of energy corresponding to the frequency $\omega_{\boldsymbol{k}}$. Importantly Eq. (S49) is quadratic in the electric field amplitude $\mathscr{A}_{\boldsymbol{k}}$, which implies that each $\boldsymbol{k}$ mode corresponds to a harmonic oscillator. If we wish to quantize the energy in quanta of $\omega_{\boldsymbol{k}}$,

$$H_{SP,\boldsymbol{k}} = \frac{\omega(\boldsymbol{k})}{2}(\alpha_{\boldsymbol{k}}\alpha^*_{\boldsymbol{k}} + \alpha^*_{\boldsymbol{k}}\alpha_{\boldsymbol{k}}), \tag{S51}$$

we can define $\alpha_{\boldsymbol{k}}$ so that,

$$\mathscr{A}_{\boldsymbol{k}} = \sqrt{\frac{\omega(\boldsymbol{k})}{SL_{\boldsymbol{k}}}}\alpha_{\boldsymbol{k}}. \tag{S52}$$

Other multiplicative phase factors in this amplitude definition (U(1) gauge choice) do not affect the quantization. Promoting the complex amplitudes to operators, $\alpha_{\boldsymbol{k}} \to a_{\boldsymbol{k}}$ and $\alpha^*_{\boldsymbol{k}} \to a^\dagger_{\boldsymbol{k}}$ with $[a_{\boldsymbol{k}}, a^\dagger_{\boldsymbol{k}}] = 1$,

$$\begin{aligned} H_{SP,\boldsymbol{k}} &= \frac{\omega(\boldsymbol{k})}{2}(a_{\boldsymbol{k}} a^\dagger_{\boldsymbol{k}} + a^\dagger_{\boldsymbol{k}} a_{\boldsymbol{k}}) \\ &= \omega(\boldsymbol{k})\Big(a_{\boldsymbol{k}} a^\dagger_{\boldsymbol{k}} + \frac{1}{2}\Big). \end{aligned} \tag{S53}$$

To summarize, we have normalized each $\boldsymbol{k}$ mode in Eqs. (S48a) and (S48b) by associating energy quanta $\omega_{\boldsymbol{k}}$ to a SP excitation in such mode. Finally, the final electric field and magnetic induction are superpositions of amplitudes in such modes,

$$\vec{\mathscr{E}} = \sum_{\boldsymbol{k}} \mathscr{A}_{\boldsymbol{k}} \vec{E}(\boldsymbol{k}). \tag{S54a}$$

$$\vec{\mathscr{B}} = \sum_{\boldsymbol{k}} \mathscr{A}_{\boldsymbol{k}} \vec{B}(\boldsymbol{k}). \tag{S54b}$$

Promoting these amplitudes to operators (in the Heisenberg picture) and using Eq. (S52),

$$\begin{aligned} \hat{\vec{\mathscr{E}}}(\boldsymbol{r}, t) &= \sum_{\boldsymbol{k}} 2\sqrt{\frac{\omega(\boldsymbol{k})}{2\epsilon_0 S L_{\boldsymbol{k}}}}\, a_{\boldsymbol{k}} \vec{E}(\boldsymbol{k}) \\ &= \sum_{\boldsymbol{k}} \sqrt{\frac{\omega(\boldsymbol{k})}{2\epsilon_0 S L_{\boldsymbol{k}}}}\, a_{\boldsymbol{k}} \vec{E}(\boldsymbol{k}) + \sqrt{\frac{\omega(\boldsymbol{k})}{2\epsilon_0 S L_{\boldsymbol{k}}}}\, a^\dagger_{\boldsymbol{k}} \vec{E}^*(\boldsymbol{k}), \end{aligned} \tag{S55a}$$

$$\hat{\vec{\mathscr{B}}}(\boldsymbol{r}, t) = \sum_{\boldsymbol{k}} \sqrt{\frac{\omega(\boldsymbol{k})}{2\epsilon_0 S L_{\boldsymbol{k}}}}\, a_{\boldsymbol{k}} \vec{B}(\boldsymbol{k}) + \sqrt{\frac{\omega(\boldsymbol{k})}{2\epsilon_0 S L_{\boldsymbol{k}}}}\, a^\dagger_{\boldsymbol{k}} \vec{B}^*(\boldsymbol{k}), \tag{S55b}$$

where we have used the fact that $\vec{\mathscr{E}}$ and $\vec{\mathscr{B}}$ are real valued to write the operators in a more conventionally symmetric form.

G. Perturbation expansion of $L_{\boldsymbol{k}}$

The fields deduced in Sec. I E are only correct up to $O(g)$, so it is important that we keep $L_{\boldsymbol{k}}$ up to that order too. Importantly, since $(\overleftrightarrow{\epsilon}_{MO})_{r\theta} = ig$ and $E_{\theta d} \propto g$, the lowest order contribution to $L_{\boldsymbol{k}}$ appears at $O(g^2)$. Hence, we do not need to take the anisotropic effects of ϵ_{MO} into account, and we can set $g = 0$ in Eq. (S7), i.e. $\overleftrightarrow{\epsilon}_{MO} \approx \epsilon_d \mathbb{I}$, where $\mathbb{I}$ is the 3×3 identity matrix. Therefore, the calculation for $L_{\boldsymbol{k}} \approx L_{\boldsymbol{k}0}$ reduces to that of the standard SP mode in the absence of external magnetic field (α_{d0} and α_{m0} are purely real) [16],

$$\begin{aligned} L_{\boldsymbol{k}0} &= \sum_i \left\{ \left[\epsilon_0 \epsilon_d |E_{i,d0}|^2 + \frac{1}{\mu_0 \mu} |B_{i,d0}|^2 \right] \frac{1}{2\epsilon_0 \alpha_{d0}} + \left[\epsilon_0 \frac{d(\omega \epsilon_{m0}(\omega))}{d\omega}\bigg|_{\omega=\frac{\Omega_0}{c}} |E_{i,m0}|^2 + \frac{1}{\mu_0 \mu} |B_{i,m0}|^2 \right] \frac{1}{2\epsilon_0 \alpha_{m0}} \right\} \\ &= \left[\epsilon_d \left(1 + \frac{k^2}{\alpha_{d0}^2}\right) + \left(\frac{\epsilon_d \Omega_0}{\alpha_{d0}}\right)^2 \right] \frac{1}{2\alpha_{d0}} + \left[\frac{d(\omega \epsilon_{m0}(\omega))}{d\omega}\bigg|_{\omega=\frac{\Omega_0}{c}} \left(1 + \frac{k^2}{\alpha_{m0}^2}\right) + \left(\frac{\epsilon_d \Omega_0}{\alpha_{d0}}\right)^2 \right] \frac{1}{2\alpha_{m0}} \\ &= \frac{-\epsilon_{m0}}{\alpha_{d0}} + \frac{1}{2\alpha_{m0}} \left[\frac{d(\omega \epsilon_{m0}(\omega))}{d\omega}\bigg|_{\omega=\frac{\Omega_0}{c}} \left(\frac{\epsilon_{m0} - \epsilon_d}{\epsilon_{m0}}\right) - \epsilon_{m0} - \epsilon_d \right]. \end{aligned} \tag{S56}$$

In this derivation, we have used $\mu = 1$, $\epsilon_0 \mu_0 = c^{-2}$, Eqs. (S27), (S35a), and (S35b) as well as the expressions for (S24b), and (S24c). [3]

[3] The final result in Eq. (S56) is twice of what is reported in the Supplementary Material of [16]. We believe our derivation has the correct prefactors; however, the use of either result gives the same order of magnitude of the effects we are interested in.

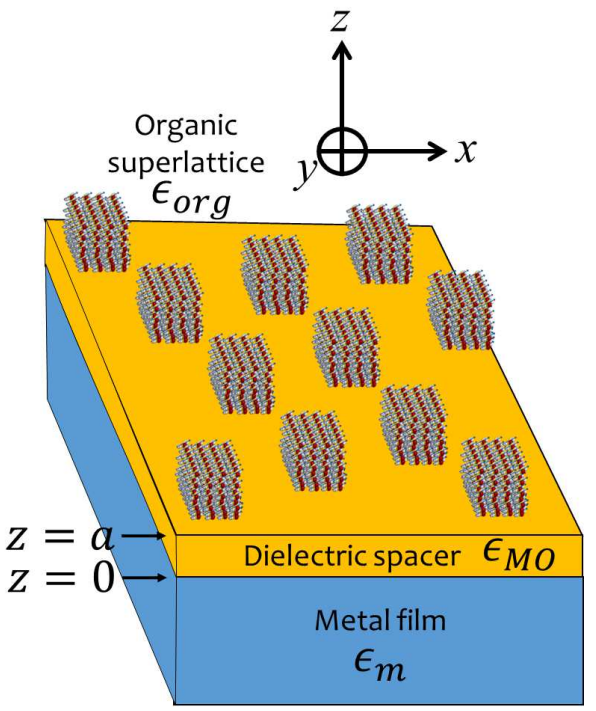

Figure S3. *Three-layer (metal-MO dielectric-organic) setup.* We are interested in the (magneto)-SP modes arising at the dielectric-organic interface ($z = a$) upon application of a perpendicular external magnetic field.

II. MAGNETO-SPS IN A THREE-LAYER SETUP

We shall now adapt the results from the previous sections to the situation where the MO layer has a finite height a, and an organic layer of isotropic dielectric ϵ_{org} is placed on top of it (see Fig. S3). As far as we are aware, the resulting expressions for the corresponding magneto-SPs have not appeared before in the literature.

A. Electromagnetic modes for each layer

1. *Organic layer ($z > a$)*

Just as we did for the MO and the metal layers (see Eqs. (S10) and (S15)), Eq. (S9) for the organic layer can be expressed in matrix form $\mathbb{M}_{org}\boldsymbol{E}_{org} = 0$,

$$\begin{bmatrix} \epsilon_m - \Omega^{-2}k_{z,org}^2 & 0 & \Omega^{-2}kk_{z,org} \\ 0 & \epsilon_m - \Omega^{-2}(k^2 + k_{z,org}^2) & 0 \\ kk_{z,org}\Omega^{-2} & 0 & \epsilon_m - \Omega^{-2}k^2 \end{bmatrix} \begin{bmatrix} E_{k,org} \\ E_{\theta,org} \\ E_{z,org} \end{bmatrix} = \begin{bmatrix} 0 \\ 0 \\ 0 \end{bmatrix}. \tag{S57}$$

Importantly, we do not fix the radial component $E_{k,org}$ to 1 because of the boundary conditions at the organic crystal and MO interface at $z = a$[4]. The corresponding secular equation for the decaying field for $z > a$, with $k_{z,org} = i\alpha_{org}$ yields

$$\alpha_{org} = \sqrt{k^2 - \Omega^2\epsilon_{org}}, \tag{S58}$$

[4] In our (arbitrary) normalization before quantization, we may set only one of the field components in one of the layers to 1, and our convention is to choose $E_{r,m} = 1$ as in the two-layer case. The rest of the fields are not arbitrary and satisfy the wave equation Eq. (S9) as well as boundary conditions at each of the interfaces.

as expected (see Eq. (S16)). Finally, just like in the metal layer, Eq. (S57) tells us that

$$E_{z,org} = \frac{ik}{\alpha_{org}} E_{r,org}, \tag{S59}$$

but does not inform us about the tangential component $E_{\theta,org}$ (nor about $E_{k,org}$), The missing components will be deduced by matching the boundary at $z = a$. Altogether, the fields in the organic layer read like those in Eqs. (S18a) and (S18b),

$$\begin{aligned}
\vec{E}_{org} &= \boldsymbol{E}_{org}\eta e^{-\alpha_{org}z} \\
&= (E_{k,org}, E_{\theta,m}, E_{z,m})\eta e^{\alpha_m z}, && \text{(S60a)} \\
\vec{B}_{org} &= \boldsymbol{B}_{org}\eta e^{-\alpha_{org}z} \\
&= \frac{-i}{\omega}(\alpha_{org}E_{\theta,org}, -ikE_{z,org} - \alpha_{org}E_{k,org}, ikE_{\theta,org})\eta e^{-\alpha_{org}z}, && \text{(S60b)}
\end{aligned}$$

denoting exponentially decreasing fields.

2. MO layer ($a > z > 0$)

For the MO layer, we translate Eqs. (S18a) and (S18b) to this setup,

$$\begin{aligned}
\vec{E}^{\pm}_{MO\downarrow} &= \boldsymbol{E}^{\pm}_{MO\downarrow}\eta e^{-\alpha^{\pm}z} \\
&= (1, E^{\pm}_{\theta,MO\downarrow}, E^{\pm}_{z,MO\downarrow})\eta e^{-\alpha^{\pm}z}, && \text{(S61a)} \\
\vec{B}^{\pm}_{MO\downarrow} &= \boldsymbol{B}^{\pm}_{MO\downarrow}\eta e^{-\alpha^{\pm}z} \\
&\quad \frac{-i}{\omega}(\alpha^{\pm}E^{\pm}_{\theta,MO\downarrow}, -ikE^{\pm}_{z,MO\downarrow} - \alpha^{\pm}, ikE^{\pm}_{\theta,MO\downarrow})\eta e^{-\alpha^{\pm}z}, && \text{(S61b)}
\end{aligned}$$

where $\vec{E}^{\pm}_{MO\downarrow}$ and $\vec{B}^{\pm}_{MO\downarrow}$ indicate exponentially decreasing fields ($k_z = i\alpha^{\pm}_{MO}$), and by slightly adapting these expressions,

$$\begin{aligned}
\vec{E}^{\pm}_{MO\uparrow} &= \boldsymbol{E}^{\pm}_{MO\uparrow}\eta e^{\alpha^{\pm}z} \\
&= (1, E^{\pm}_{\theta,MO\uparrow}, E^{\pm}_{z,MO\uparrow})\eta e^{\alpha^{\pm}z}, && \text{(S62a)} \\
\vec{B}^{\pm}_{MO\uparrow} &= \boldsymbol{B}^{\pm}_{MO\uparrow}\eta e^{\alpha^{\pm}z} \\
&\quad \frac{-i}{\omega}(-\alpha^{\pm}E^{\pm}_{\theta,MO\uparrow}, -ikE^{\pm}_{z,MO\uparrow} + \alpha^{\pm}, ikE^{\pm}_{\theta,MO\uparrow})\eta e^{\alpha^{\pm}z}, && \text{(S62b)}
\end{aligned}$$

where $\vec{E}^{\pm}_{MO\uparrow}$ and $\vec{B}^{\pm}_{MO\uparrow}$ denote exponentially increasing fields ($k_z = -i\alpha^{\pm}_{MO}$). In previous sections where MO was considered to fill up all the space $z > 0$, the latter fields were not considered, the reason being that $e^{\alpha^{\pm}_{MO}z}$ was unbounded as $z \to \infty$; this is not the case when the largest value of z is a [5]. Hence, the analogous expressions to Eqs. (S19a) and (S19b) are,

$$\begin{aligned}
\vec{E}_{MO} &= t^{+}_{\downarrow}\vec{E}^{+}_{MO\downarrow} + t^{-}_{\downarrow}\vec{E}^{-}_{MO\downarrow} + t^{+}_{\uparrow}\vec{E}^{+}_{MO\uparrow} + t^{-}_{\uparrow}\vec{E}^{-}_{MO\uparrow}, && \text{(S63a)} \\
\vec{B}_{MO} &= t^{+}_{\downarrow}\vec{B}^{+}_{MO\downarrow} + t^{-}_{\downarrow}\vec{B}^{-}_{MO\downarrow} + t^{+}_{\uparrow}\vec{B}^{+}_{MO\uparrow} + t^{-}_{\uparrow}\vec{B}^{-}_{MO\uparrow}. && \text{(S63b)}
\end{aligned}$$

where $t^{\pm}_{\downarrow}$ and $t^{\pm}_{\uparrow}$ are the unknown coefficients. Here, $E^{\pm}_{\theta,MO\downarrow} = E^{\pm}_{\theta,MO\uparrow} = E^{\pm}_{\theta,MO}$ but $E^{\pm}_{z,MO\downarrow} = -E^{\pm}_{z,MO\uparrow} = E^{\pm}_{z,MO}$. These identities are easy to check as $\vec{E}^{\pm}_{MO\downarrow}$ is associated with $k_z = i\alpha^{\pm}_{MO}$ and $\vec{E}^{\pm}_{MO\uparrow}$ with $k_z = -i\alpha^{\pm}_{MO}$, but Eqs. (S14a) and (S14b) were derived for $k_z = i\alpha^{\pm}_{MO}$.

---

[5] A more intuitive way to describe this situation is that $\vec{E}^{\pm}_{BIG\downarrow}$ and $\vec{B}^{\pm}_{BIG\downarrow}$ denote fields that exponentially decrease starting from $z = 0$ going upwards; similarly, $\vec{E}^{\pm}_{BIG\uparrow}$ and $\vec{B}^{\pm}_{BIG\uparrow}$ describe exponentially decreasing fields starting from $z = a$ going downwards.

3. *Metal layer ($z < 0$)*

Finally, for the metal layer, all the expressions we derived in Sec. I hold, in particular Eqs. (S20a) and (S20b); we still assume $E_{k,m} = 1$.

B. Matching the modes at the boundaries ($z = 0$ and $z = a$)

Given this prelude, the analogous boundary conditions to Eqs. (S21a)–(S21f) for $z = 0$ are,

$$1 = t^+_{MO\downarrow} + t^-_{MO\downarrow} + t^+_{MO\uparrow} + t^-_{MO\uparrow}, \tag{S64a}$$

$$E_{\theta,m} = t^+_{MO\downarrow}E^+_{\theta,MO\downarrow} + t^-_{MO\downarrow}E^-_{\theta,MO\downarrow} + t^+_{MO\uparrow}E^+_{\theta,MO\uparrow} + t^-_{MO\uparrow}E^-_{\theta,MO\uparrow}, \tag{S64b}$$

$$\epsilon_m E_{z,m} = \epsilon_d(t^+_{MO\downarrow}E^+_{z,MO\downarrow} + t^-_{MO\downarrow}E^-_{z,MO\downarrow} + t^+_{MO\uparrow}E^+_{z,MO\uparrow} + t^-_{MO\uparrow}E^-_{z,MO\uparrow}), \tag{S64c}$$

$$\alpha_m E_{\theta,m} = -(\alpha^+_{MO}t^+_{MO\downarrow}E^+_{\theta,MO\downarrow} + \alpha^-_{MO}t^-_{MO\downarrow}E^-_{\theta,MO\downarrow}) + (\alpha^+_{MO}t^+_{MO\uparrow}E^+_{\theta,MO\uparrow} + \alpha^-_{MO}t^-_{MO\uparrow}E^-_{\theta,MO\uparrow}), \tag{S64d}$$

$$\begin{aligned} kE_{z,m} + i\alpha_m = {} & k(t^+_{MO\downarrow}E^+_{z,MO\downarrow} + t^-_{MO\downarrow}E^-_{z,MO\downarrow} + t^+_{MO\uparrow}E^+_{zMO\uparrow} + t^-_{MO\uparrow}E^-_{z,MO\uparrow}) \\ & - i\alpha^+_{MO}(t^+_{MO\downarrow} - t^+_{MO\uparrow}) - i\alpha^-_{MO}(t^-_{MO\downarrow} - t^-_{MO\uparrow}), \end{aligned} \tag{S64e}$$

$$E_{\theta,m} = t^+_{MO\downarrow}E^+_{\theta,MO\downarrow} + t^-_{MO\downarrow}E^-_{\theta,MO\downarrow} + t^+_{MO\uparrow}E^+_{\theta,MO\uparrow} + t^-_{MO\uparrow}E^-_{\theta,MO\uparrow}, \tag{S64f}$$

whereas for $z = a$ they are,

$$E_{k,org} = t^+_{MO\downarrow}\chi^+ + t^-_{MO\downarrow}\chi^- + t^+_{MO\uparrow}\frac{1}{\chi^+} + t^-_{MO\uparrow}\frac{1}{\chi^-}, \tag{S65a}$$

$$E_{\theta,org} = t^+_{MO\downarrow}E^+_{\theta,MO\downarrow}\chi^+ + t^-_{MO\downarrow}E^-_{\theta,MO\downarrow}\chi^- + t^+_{MO\uparrow}E^+_{\theta,MO\uparrow}\frac{1}{\chi^+} + t^-_{MO\uparrow}E^-_{\theta,MO\uparrow}\frac{1}{\chi^-}, \tag{S65b}$$

$$\epsilon_{org}E_{z,org} = \epsilon_d\left(t^+_{MO\downarrow}E^+_{z,MO\downarrow}\chi^+ + t^-_{MO\downarrow}E^-_{z,MO\downarrow}\chi^- + t^+_{MO\uparrow}E^+_{z,MO\uparrow}\frac{1}{\chi^+} + t^-_{MO\uparrow}E^-_{z,MO\uparrow}\frac{1}{\chi^-}\right), \tag{S65c}$$

$$\begin{aligned} -\alpha_{org}E_{\theta,org} = {} & -\left(\alpha^+_{MO}t^+_{MO\downarrow}E^+_{\theta,MO\downarrow}\chi^+ + \alpha^-_{MO}t^-_{MO\downarrow}E^-_{\theta,MO\downarrow}\chi^-\right) \\ & + \left(\alpha^+_{MO}t^+_{MO\uparrow}E^+_{\theta,MO\uparrow}\frac{1}{\chi^+} + \alpha^-_{MO}t^-_{MO\uparrow}E^-_{\theta,MO\uparrow}\frac{1}{\chi^-}\right), \end{aligned} \tag{S65d}$$

$$\begin{aligned} kE_{z,org} - i\alpha_{org}E_{r,org} = {} & k\left(t^+_{MO\downarrow}E^+_{z,MO\downarrow}\chi^+ + t^-_{MO\downarrow}E^-_{z,MO\downarrow}\chi^- + t^+_{MO\uparrow}E^+_{z,MO\uparrow}\frac{1}{\chi^+} + t^-_{MO\uparrow}E^-_{z,MO\uparrow}\frac{1}{\chi^-}\right) \\ & - i\alpha^+_{MO}\left(t^+_{MO\downarrow}\chi^+ - t^+_{MO\uparrow}\frac{1}{\chi^+}\right) - i\alpha^-_{MO}\left(t^-_{MO\downarrow}\chi^- - t^-_{MO\uparrow}\frac{1}{\chi^-}\right), \end{aligned} \tag{S65e}$$

$$E_{\theta,org} = t^+_{MO\downarrow}E^+_{\theta,MO\downarrow}\chi^+ + t^-_{MO\downarrow}E^-_{\theta,MO\downarrow}\chi^- + t^+_{MO\uparrow}E^+_{\theta,MO\uparrow}\frac{1}{\chi^+} + t^-_{MO\uparrow}E^-_{\theta,MO\uparrow}\frac{1}{\chi^-}. \tag{S65f}$$

Here, $\chi^\pm = e^{-\alpha^\pm_{MO}a}$ embodies the vertical thickness dependence of the problem. Eqs. (S64a)–(S65f) can be manipulated to yield an entirely analogous expression to Eq. (S22). This resulting expression can then be perturbatively expanded in g and the analogous procedure of Sec. I E follows, with the caveat that the algebra becomes much more laborious. We bypass the latter by automatizing such work with Wolfram Mathematica(c). We summarize the results in the following subsections.

C. Perturbation expansion on g

1. *Solving for $t^\pm_\downarrow$ and $t^\pm_\uparrow$*

It is clear that provided that the frequencies Ω_0 and Ω_2 are modified accordingly (one finds $\Omega_1 = 0$ again), the expansions for the dielectric constants and the wavevectors can all be recycled from Sec. I E. On top of these quantities, following Sec.

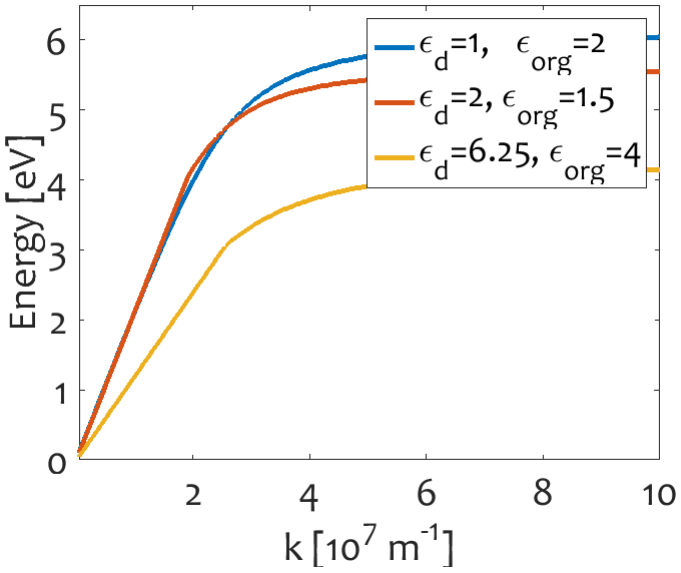

Figure S4. *SP dispersion energy as a function of $k = |\boldsymbol{k}|$ for the three-layer (metal-MO dielectric-organic) setup, assuming $g = 0$.* Plots generated using Eq. (S69) with Drude parameters for Ag, $\epsilon_\infty \sim 4$, $\omega_P \sim 9$ eV, and varying the dielectric permittivity ϵ_d as well as that of the organic layer. Since $\Omega = \Omega_0 + O(g^2)$, the plots are correct up to $O(g)$, which is our perturbation order of interest. Just like with Fig. (S2), notice that the dispersion curves start-off linearly (light-like excitations), but plateau to constant values at large wavevectors (charge oscillations in the metal), which become smaller as the dielectric permittivity increases.

I E, we ought to expand α_{org} and $\chi^\pm$ up to $O(g^2)$ in Eq. (S58),

$$\alpha_{org} \approx \alpha_{org0} + g^2 \alpha_{org22} \Omega_2, \tag{S66a}$$

$$\alpha_{org0} = \sqrt{k^2 - \Omega_0^2 \epsilon_{org}}, \tag{S66b}$$

$$\alpha_{org22} = -\frac{\Omega_0 \epsilon_{org}}{\alpha_{org0}}, \tag{S66c}$$

$$\chi^\pm \approx \chi_0 \left\{ 1 \mp a g \alpha_{d1} - g^2 \left[a^2 \frac{\alpha_{d1}^2}{2} + a(\alpha_{d20} + \alpha_{d22}\Omega_2) \right] \right\}, \tag{S67}$$

but we only need $t^\pm_{MO\downarrow}$ and $t^\pm_{MO\uparrow}$ up to $O(g)$,

$$t^\pm_{MO\downarrow} \approx t_{d\downarrow 0} \pm g\, t_{d\downarrow 1}, \tag{S68a}$$

$$t^\pm_{MO\uparrow} \approx t_{d\uparrow 0} \pm g\, t_{d\uparrow 1}. \tag{S68b}$$

Collecting the zeroth-order in g contributions in Eqs. (S64a)–(S65f), we derive an implicit equation for Ω_0 which coincides with the standard textbook result for a three-layer system in the absence of an external magnetic field [14],

$$\chi_0^2 = \left(\frac{\alpha_{d0}\epsilon_{m0} + \alpha_{m0}\epsilon_d}{\alpha_{d0}\epsilon_{m0} - \alpha_{m0}\epsilon_d} \right) \left(\frac{\alpha_{d0}\epsilon_{org} + \alpha_{org0}\epsilon_d}{\alpha_{d0}\epsilon_{org} - \alpha_{org0}\epsilon_d} \right), \tag{S69}$$

where α_{d0}, α_{m0}, α_{org0}, and ϵ_{m0} are all functions of Ω_0. This equation is the analogue of Eqs. (S27) and (S28) for three layers. It is not possible to explicitly solve for Ω_0, but one can readily compute it numerically from such implicit equation (see Fig. S4). The formula for Ω_2 is too long to display it here and is, anyway, not relevant on its own. However, we make use of it to obtain our final results.

Next, we compute the coefficients in Eqs. (S68a) and (S68b) in analogy to the two-layer case in Eqs. (S36) and (S37). At zeroth-order in g,

$$t_{d\downarrow 0} = \frac{\alpha_{m0}\epsilon_d - \alpha_{d0}\epsilon_{m0}}{4\alpha_{m0}\epsilon_d}, \tag{S70a}$$

$$t_{d\uparrow 0} = \frac{\alpha_{m0}\epsilon_d + \alpha_{d0}\epsilon_{m0}}{4\alpha_{m0}\epsilon_d}, \tag{S70b}$$

while their first-order in g corrections are,

$$\begin{aligned} t_{d\downarrow 1} = \alpha_{d1}\Big(& a\alpha_{d0}^3(\chi_0^2-1)\epsilon_{m0} \\ & -\alpha_{d0}^2\{\chi_0^2[a\epsilon_{m0}(\alpha_{m0}+\alpha_{org0}) + a\alpha_{m0}\epsilon_d + \epsilon_{m0}] + a\alpha_{m0}\epsilon_d - a\alpha_{m0}\epsilon_{m0} + a\alpha_{org0}\epsilon_{m0} - \epsilon_{m0}\} \\ & +\alpha_{d0}\{a\alpha_{m0}^2(\chi_0^2+1)\epsilon_d + \alpha_{m0}(a\alpha_{org0}+1)[\chi_0^2(\epsilon_d+\epsilon_{m0}) - \epsilon_d + \epsilon_{m0}] + 2\alpha_{org0}\epsilon_{m0}\} \\ & -\alpha_{m0}^2(\chi_0^2-1)\epsilon_d(a\alpha_{org0}+1)\Big)/ \\ & \{4\alpha_{m0}\epsilon_d[\chi_0^2(\alpha_{m0}-\alpha_{d0})(\alpha_{d0}-\alpha_{org0}) + (\alpha_{d0}+\alpha_{m0})(\alpha_{d0}+\alpha_{org0})]\} \end{aligned} \tag{S71a}$$

and

$$\begin{aligned} t_{d\uparrow 1} = \Big[& \alpha_{d1}\chi_0^2\Big(\alpha_{d0}\epsilon_{m0}\{a\alpha_{d0}^2 - \alpha_{org0}[a(\alpha_{d0}+\alpha_{m0})+2] + a\alpha_{d0}\alpha_{m0} + \alpha_{d0} - \alpha_{m0}\} \\ & -\alpha_{m0}\epsilon_d(\alpha_{d0}+\alpha_{m0})[a(\alpha_{d0}-\alpha_{org0})-1]\Big) \\ & -\alpha_{d1}(\alpha_{d0}+\alpha_{m0})[a(\alpha_{d0}+\alpha_{org0})+1](\alpha_{d0}\epsilon_{m0}+\alpha_{m0}\epsilon_d)\Big]/ \\ & \{4\alpha_{m0}\epsilon_d[\chi_0^2(\alpha_{m0}-\alpha_{d0})(\alpha_{d0}-\alpha_{org0}) + (\alpha_{d0}+\alpha_{m0})(\alpha_{d0}+\alpha_{org0})]\}. \end{aligned} \tag{S71b}$$

Hence, at zeroth order, $t^+_{MO\downarrow} + t^-_{MO\downarrow} = 2t_{d\downarrow 0}$ and $t^+_{MO\uparrow} + t^-_{MO\uparrow} = 2t_{d\uparrow 0}$, and these total coefficients for exponentially decreasing and increasing fields become identical to the textbook results for SP modes in the three-layer setup in the absence of an external magnetic field.

2. *Collecting the expressions for the fields*

For reference, the zeroth-order fields are given by,

$$\vec{E}_{org0} = (E_{k,org0}, 0, E_{z,org0})\eta_0 e^{-\alpha_{org0}z}, \tag{S72a}$$

$$\vec{B}_{org0} = (0, B_{\theta,org0}, 0)\eta_0 e^{-\alpha_{org0}z}, \tag{S72b}$$

$$\vec{E}_{d0} = 2t_{d\downarrow 0}(1, 0, E_{z,d\downarrow 0})\eta_0 e^{-\alpha_{d0}z} + 2t_{d\uparrow 0}(1, 0, E_{z,d\uparrow 0})\eta_0 e^{\alpha_{d0}z}, \tag{S72c}$$

$$\vec{B}_{d0} = 2t_{d\downarrow 0}(0, B_{\theta,d\downarrow 0}, 0)\eta_0 e^{-\alpha_{d0}z} + 2t_{d\uparrow 0}(0, B_{\theta,d\uparrow 0}, 0)\eta_0 e^{\alpha_{d0}z}, \tag{S72d}$$

$$\vec{E}_{m0} = (1, 0, E_{z,m0})\eta_0 e^{-\alpha_{m0}z}, \tag{S72e}$$

$$\vec{B}_{m0} = (0, B_{\theta,m0}, 0)\eta_0 e^{-\alpha_{m0}z}, \tag{S72f}$$

with each of the components being,

$$E_{k,org0} = \frac{\alpha_{m0}(\chi_0^2+1)\epsilon_d - \alpha_{d0}(\chi_0^2-1)\epsilon_{m0}}{2\alpha_{m0}\chi_0\epsilon_d}, \tag{S73a}$$

$$E_{z,org0} = -\frac{ik[\alpha_{d0}(\chi_0^2+1)\epsilon_{m0} + \alpha_{m0}(\epsilon_d - \chi_0^2\epsilon_d)]}{2\alpha_{d0}\alpha_{m0}\chi_0\epsilon_{org}}, \tag{S73b}$$

$$B_{\theta,org0} = \frac{i\{2\alpha_{d0}\alpha_{m0}\alpha_{org0}\chi_0\epsilon_{org} + k^2[\alpha_{d0}(\chi_0^2+1)\epsilon_{m0} + \alpha_{m0}(\epsilon_d - \chi_0^2\epsilon_d)]\}}{2\alpha_{d0}\alpha_{m0}\chi_0\Omega_0 c\epsilon_{org}}, \tag{S73c}$$

$$E_{z,d\downarrow 0} = -E_{z,d\uparrow 0} = \frac{ik}{\alpha_{d0}}, \tag{S73d}$$

$$B_{\theta,d\downarrow 0} = -B_{\theta,d\uparrow 0} = -\frac{i(k^2-\alpha_{d0}^2)}{\alpha_{d0}\Omega_0 c}, \tag{S73e}$$

$$E_{z,m0} = -\frac{ik}{\alpha_{m0}}, \tag{S73f}$$

$$B_{\theta,m0} = \frac{i(k^2-\alpha_{m0}^2)}{\alpha_{m0}\Omega_0 c}. \tag{S73g}$$

The expressions for the $O(g)$ fields at each layer are also cumbersome; we only show the electric field in the organic layer, as it is the one associated with the coupling with excitons (see Eq. (S39a)),

$$\vec{E}_{org} \approx \vec{E}_{org0} + g\vec{E}_{org1}. \tag{S74}$$

The first order in g contribution is

$$\vec{E}_{org1} = \boldsymbol{E}_{org1}\eta_0 e^{-\alpha_{org0}z}, \tag{S75}$$

where $\boldsymbol{E}_{org1}$ is purely tangential and purely-imaginary valued,

$$\begin{aligned}\boldsymbol{E}_{org1}\cdot\hat{\boldsymbol{\theta}} = -i\Omega_0^2\Big(&\alpha_{m0}\epsilon_d\{a[\chi_0^2(\alpha_{d0}-\alpha_{org0})+\alpha_{d0}+\alpha_{org0}]-\chi_0^2+1\}\\ &+\epsilon_{m0}\{\chi_0^2[a\alpha_{d0}(\alpha_{org0}-\alpha_{d0})+\alpha_{org0}]+a\alpha_{d0}(\alpha_{d0}+\alpha_{org0})-\alpha_{org0}\}\Big)/\\ &2\alpha_{m0}\epsilon_d[\chi_0^2(\alpha_{m0}-\alpha_{d0})(\alpha_{d0}-\alpha_{org0})+(\alpha_{d0}+\alpha_{m0})(\alpha_{d0}+\alpha_{org0})].\end{aligned} \tag{S76}$$

Compared with Eq. (S41a), the z-dependence of $\vec{E}_{org1}$ is purely exponential, as the lowest order correction of α_{org} to α_{org0} is $O(g^2)$.

D. Quantization and normalization of modes

Equipped with these results, we use Eqs. (S64a)–(S65f) to compile expressions for the fields in each layer. First, we aim to compute the vertical normalization length $L_{\boldsymbol{k}}$ for each mode. In analogy to Eq. (S50), we obtain,

$$\begin{aligned}L_{\boldsymbol{k}} = &\sum_i\left[\epsilon_0\epsilon_{org}|E_{i,org}|^2+\frac{1}{\mu_0\mu}|B_{i,org}|^2\right]\frac{1}{\epsilon_0}\int_a^\infty dz e^{-(\alpha_{org}^*+\alpha_{org})z}\\ &+\sum_{ij}\sum_{\gamma,\delta\in\{+,-\}}\sum_{u,v\in\{\uparrow,\downarrow\}}(t_{MOu}^\gamma)^* t_{MOv}^\delta\left[\epsilon_0(\epsilon_{MO,ij}E_{j,MO}^\gamma)^* E_{i,MO}^\delta+\frac{1}{\mu_0\mu}(B_{i,MO}^\gamma)^* B_{i,MO}^\delta\right]\\ &\quad\times\frac{1}{\epsilon_0}\int_0^a dz e^{[(\mathrm{sgn}(u)(\alpha_{MO}^\gamma)^*+\mathrm{sgn}(v)\alpha_{MO}^\delta]z}\\ &+\sum_i\left[\epsilon_0\frac{d(\omega\epsilon_m(\omega))}{d\omega}|E_{i,m}|^2+\frac{1}{\mu_0\mu}|B_{i,m}|^2\right]\frac{1}{\epsilon_0}\int_{-\infty}^0 dz e^{(\alpha_m^*+\alpha_m)z},\end{aligned} \tag{S77}$$

where $\mathrm{sgn}(\uparrow) = -\mathrm{sgn}(\downarrow) = 1$ denote the exponentially increasing or decreasing fields, respectively. At $O(g)$, $L_{\boldsymbol{k}} \approx L_{\boldsymbol{k}0}$ as in Eq. (S56), and the anisotropy of the MO layer is unimportant. Carrying out the integrations explicitly (and taking care of the possibility that α_{d0} is complex-valued),

$$\begin{aligned}
L_{\boldsymbol{k}0} = &\sum_i \left[\epsilon_0\epsilon_{org}|E_{i,org0}|^2 + \frac{1}{\mu_0\mu}|B_{i,org0}|^2\right]\frac{e^{-2\Re\alpha_{org0}a}}{2\epsilon_0\Re\alpha_{org0}} \\
&+4\sum_i \left|t_{d\uparrow 0}\right|^2\left[\epsilon_0\epsilon_d|E_{i,d\uparrow 0}|^2 + \frac{1}{\mu_0\mu}|B_{i,d\uparrow 0}|^2\right]\left(\frac{e^{2\Re\alpha_{d0}a}-1}{2\epsilon_0\Re\alpha_{d0}}\right) \\
&+4\sum_i \left|t_{d\downarrow 0}\right|^2\left[\epsilon_0\epsilon_d|E_{i,d\downarrow 0}|^2 + \frac{1}{\mu_0\mu}|B_{i,d\downarrow 0}|^2\right]\left(\frac{1-e^{-2\Re\alpha_{d0}a}}{2\epsilon_0\Re\alpha_{d0}}\right) \\
&+\left\{4\sum_{ij}(t_{d\uparrow 0})^*(t_{d\downarrow 0})\left[\epsilon_0\sum_i\epsilon_d(E_{i,d\uparrow 0})^*E_{i,d\downarrow 0} + \frac{1}{\mu_0\mu}(B_{i,d\uparrow 0})^*B_{i,d\downarrow 0}\right]\left(\frac{a}{\epsilon_0}\right) + \text{c.c.}\right\} \\
&+\sum_i\left[\epsilon_0\frac{d(\omega\epsilon_m(\omega))}{d\omega}|E_{i,m0}|^2 + \frac{1}{\mu_0\mu}|B_{i,m0}|^2\right]\frac{1}{2\epsilon_0\Re\alpha_{m0}},
\end{aligned} \tag{S78}$$

One may numerically compute $L_{\boldsymbol{k}}$ by plugging Eqs. (S70a), (S70b), and (S72a)–(S73g) into Eq. (S78). We do not display the resulting analytical expression, which anyhow, is lengthy and not particularly illuminating.

III. EXCITON-EXCITON AND EXCITON-SP COUPLINGS

In Secs. I and II, we solved for the electromagnetic profile of the magneto-SP modes in a two- and three-layer setup. We are now ready to describe the organic superlattice. We regard the latter to be either "embedded" in the MO layer (in the two layer setup) or in its separate third layer (in the three-layer one). As explained in the following paragraphs, the superlattice consists of a monoclinic array of organic aggregate nanopillars. For simplicity, we take each of the nanopillars to be a rectangular parallelepiped of volume $W_xW_yW_z$ (here, W_i is the width of the nanopillar along the i-th axis). If the nanopillar density is ρ_{np}, it contains $N_{np} = \rho_{np}W_xW_yW_z$ chromophores. Furthermore, the three-dimensional positions of the individual chromophores constituting each nanopillar are denoted,

$$\boldsymbol{r}_{\boldsymbol{m}s} = \underbrace{(m_x\delta_x\hat{\boldsymbol{x}} + m_y\delta_y\hat{\boldsymbol{y}})}_{\equiv\boldsymbol{r}_{\boldsymbol{m}}} + \underbrace{s\delta_z}_{\equiv z_s}\hat{\boldsymbol{z}}, \tag{S79}$$

where δ_i is the spacing between chromophores along the i-th direction,

A. Dipolar couplings between nanopillars

We shall first study the energetic contribution due to the excitons alone. We model this as,

$$H_{exc} = \sum_{\boldsymbol{n},s}\omega_{\boldsymbol{n}}\sigma^\dagger_{\boldsymbol{n}}\sigma_{\boldsymbol{n}} + \sum_{\boldsymbol{n}\neq\boldsymbol{n}'}(J_{\boldsymbol{n}\boldsymbol{n}'}\sigma^\dagger_{\boldsymbol{n}}\sigma_{\boldsymbol{n}'} + \text{h.c.}), \tag{S80}$$

where $\omega_{\boldsymbol{n}}$ is the bare energy of the $\boldsymbol{n}$-th collective nanopillar dipole, which we take in the ideal case to be $\omega_{\boldsymbol{n}} = \bar{\omega}$. The exciton hopping amplitude between the $\boldsymbol{n}$-th and $\boldsymbol{n}'$-th nanopillars is approximated as a near-field dipolar coupling,

$$J_{\boldsymbol{n}\boldsymbol{n}'} = \frac{\eta}{\epsilon|\boldsymbol{r}_{\boldsymbol{n}} - \boldsymbol{r}_{\boldsymbol{n}'}|^3}\left[\boldsymbol{\mu}_{\boldsymbol{n}}\cdot\boldsymbol{\mu}_{\boldsymbol{n}'} - 3(\boldsymbol{\mu}_{\boldsymbol{n}}\cdot\boldsymbol{e}_{\boldsymbol{n}\boldsymbol{n}'})(\boldsymbol{\mu}_{\boldsymbol{n}'}\cdot\boldsymbol{e}_{\boldsymbol{n}\boldsymbol{n}'})\right], \tag{S81}$$

where $\eta = 0.625\,\mathrm{meV(nm^3/D^2)}$, $\boldsymbol{e}_{\boldsymbol{n}\boldsymbol{n}'} = \frac{\boldsymbol{r}_{\boldsymbol{n}} - \boldsymbol{r}_{\boldsymbol{n}'}}{|\boldsymbol{r}_{\boldsymbol{n}} - \boldsymbol{r}_{\boldsymbol{n}'}|}$, where $\boldsymbol{r}_{\boldsymbol{n}}$ is the average in-plane location of the $\boldsymbol{n}$-th nanopillar, and we take $\epsilon \approx 1$, the dielectric permittivity in the medium surrounding the nanopillars. Eq. (S81) implicitly relies on a separation of energy scales, namely, that the coupling between chromophores is much stronger within a single nanopillar than between different ones. Hence, we start with the collective superradiant nanopillar transitions which scale as $\boldsymbol{\mu}_{\boldsymbol{n}} = \sum_{\boldsymbol{m}s}\boldsymbol{p}_{\boldsymbol{m}s} \approx \sqrt{N_{np}}\boldsymbol{p}_{\boldsymbol{n}}$, where $\boldsymbol{p}_{\boldsymbol{m}s}$ is the transition dipole moment of the $\boldsymbol{m}s$-th chromophore in the nanopillar, the sum is over all $\boldsymbol{m}s$ values associated with the $\boldsymbol{n}$-th nanopillar, and $\boldsymbol{p}_{\boldsymbol{m}s} = \boldsymbol{p}_{\boldsymbol{n}}$, that is, we take the dipole to be equal for all chromophores within the

corresponding nanopillar. This approximation should provide a semiquantitative description of the dispersion of the organic superlattice alone. A more refined description would rely on the coupled-dipole method [17–19], but is beyond the scope of this work, as this simplified model illustrates the essence of the problem.

We shall now consider a general two-dimensional monoclinic superlattice with unit cell defined by vectors $\vec{OD}$ and $\vec{OC}$ depicted in Fig. S5. For convenience, we temporarily adopt the θ-rotated coordinate system $x'y'$ which, with respect to the original xy system, is defined by,

$$\begin{bmatrix} \hat{\boldsymbol{x}} \\ \hat{\boldsymbol{y}} \end{bmatrix} = \begin{bmatrix} \cos\theta & -\sin\theta \\ \sin\theta & \cos\theta \end{bmatrix} \begin{bmatrix} \hat{\boldsymbol{x}}' \\ \hat{\boldsymbol{y}}' \end{bmatrix}. \tag{S82}$$

We will later explain how to obtain θ. We take two sides of the parallelogram (AB and CD) to be parallel to $\hat{\boldsymbol{x}}'$. For simplicity, the nanopillars are taken to be rectangular parallelepipeds. Their transition dipoles $\boldsymbol{\mu_n} = \boldsymbol{\mu}$ are fixed in the $x'y'$ plane and make an angle α' with respect to $\hat{\boldsymbol{x}}'$ (or $\alpha \equiv \alpha' + \theta$ with respect to $\hat{\boldsymbol{x}}$). Notice that all sites are equivalent. We only account for nearest-neighbor (NN) and next-nearest-neighbor interactions (NNN). We classify the interactions as horizontal NNN (AB, CD), vertical NNN (AD, BC), diagonal type A NN (OA, OC), and diagonal type B NN (OB,OD), respectively,

$$J_h = \eta\mu^2 \frac{(1-3\cos^2\alpha')}{\Delta_h^3}, \tag{S83a}$$

$$J_v = \eta\mu^2 \frac{[1-3\cos^2(\alpha'-\beta)]}{\Delta_v^3}, \tag{S83b}$$

$$J_{diagA} = \eta\mu^2 \frac{[1-3\cos^2(\alpha'-\gamma)]}{\left(\frac{\Delta_h^2+2\Delta_h\Delta_v\cos\beta+\Delta_v^2}{4}\right)^{3/2}}, \tag{S83c}$$

$$J_{diagB} = \eta\mu^2 \frac{[1-3\cos^2(\alpha'+\delta)]}{\left(\frac{\Delta_h^2-2\Delta_h\Delta_v\cos\beta+\Delta_v^2}{4}\right)^{3/2}}. \tag{S83d}$$

Here, $|\boldsymbol{\mu}| = \mu$ and the side lengths are $\overline{AB} = \overline{CD} = \Delta_h$ and $\overline{BC} = \overline{AD} = \Delta_v$. We have also conveniently introduced the angles $\beta \equiv \angle BCD = \angle DAB$, as well as the following,

$$\gamma = \operatorname{atan}\frac{\Delta_v\sin\beta}{\Delta_h + \Delta_v\cos\beta}, \tag{S84a}$$

$$\delta = \operatorname{atan}\frac{\Delta_v\sin\beta}{\Delta_h - \Delta_v\cos\beta}. \tag{S84b}$$

Assuming that all site energies are equal, $\omega_{\boldsymbol{n}} = \bar{\omega}$, we may rewrite Eq. (S80) in $\boldsymbol{k}$ space, $H_{exc} = \sum_{\boldsymbol{k}} H_{exc,\boldsymbol{k}}$, where $H_{exc,\boldsymbol{k}} = \omega_{exc,\boldsymbol{k}}\sigma^\dagger_{\boldsymbol{k}}\sigma_{\boldsymbol{k}}$, where $\boldsymbol{k} = k_{x'}\hat{\boldsymbol{x}}' + k_{y'}\hat{\boldsymbol{y}}'$ and

$$\begin{aligned} \omega_{exc,\boldsymbol{k}} = \bar{\omega} &+ 2J_h\cos(k_{x'}\Delta_h) + 2J_v\cos\left[k_{x'}\Delta_v\cos\beta + k_{y'}\Delta_v\sin\beta\right] \\ &+ 2J_{diagA}\cos\left[k_{x'}\frac{\Delta_h+\Delta_v\cos\beta}{2} + k_{y'}\frac{\Delta_v\sin\beta}{2}\right] \\ &+ 2J_{diagB}\cos\left[k_{x'}\frac{\Delta_h-\Delta_v\cos\beta}{2} - k_{y'}\frac{\Delta_v\sin\beta}{2}\right] \end{aligned} \tag{S85}$$

is the resulting dispersion relation for the excitons alone.

As explained in the main text, we would ideally like to design a plexciton dispersion which features a global gap in the bulk. This requires a superlattice with an "H-aggregate" dispersion along all wavevector directions. Mathematically, this means that the dispersion $\omega_{exc,\boldsymbol{k}}$ should be a maximum at $\boldsymbol{k} = 0$. It turns out that this is not possible in a rectangular lattice ($\beta = \frac{\pi}{2}$), as the resulting J-couplings ($J_i < 0$) arising from the geometric constraints end up dominating the H-couplings ($J_i > 0$) at least along one direction, yielding a minimum, or at best a saddle point for $\omega_{exc,\boldsymbol{k}}$ at $\boldsymbol{k} = 0$. Hence, we proceed in a more systematic fashion. Taylor expanding Eq. (S85) up to quadratic order in $k_{i'}$,

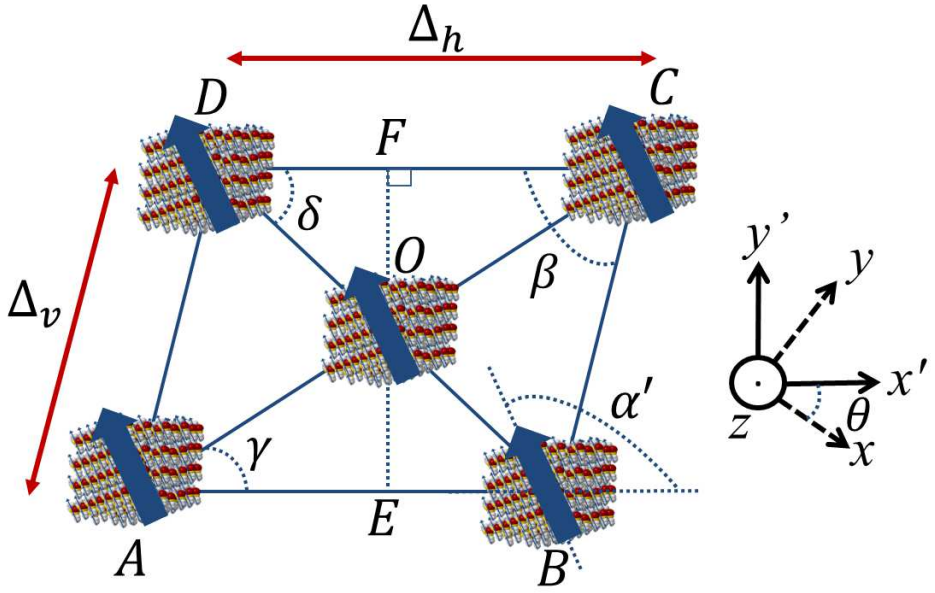

Figure S5. *Geometry of two-dimensional monoclinic superlattice of organic nanopillars.* $x'y'$ denotes a temporary Cartesian coordinate system which is rotated at θ from the original xy system. The collective transition dipole moments of the nanopillars make an angle α' with respect to $\hat{\boldsymbol{x}}'$ (or $\alpha \equiv \alpha' + \theta$ with respect to $\hat{\boldsymbol{x}}$). The horizontal and vertical distances Δ_h and Δ_v, together with the angles β, γ, and δ fully define the superlattice.

$$\omega_{exc,\boldsymbol{k}} \approx \bar{\omega}'_{eff} + \begin{bmatrix} k_{x'} & k_{y'} \end{bmatrix} \begin{bmatrix} M_{x'x'} & M_{x'y'} \\ M_{y'x'} & M_{y'y'} \end{bmatrix} \begin{bmatrix} k_{x'} \\ k_{y'} \end{bmatrix}, \tag{S86}$$

where the constant offset is obtained by evaluating $\omega_{exc,\boldsymbol{k}}$ at $\boldsymbol{k} = 0$,

$$\bar{\omega}'_{eff} = \bar{\omega} + 2J_h + 2J_v + 2J_{diagA} + 2J_{diagB}. \tag{S87}$$

Here, $M_{i'j'} = \frac{1}{2}\frac{\partial^2 E_{exc,\boldsymbol{k}}}{\partial k_{i'} \partial k_{j'}}\Big|_{\boldsymbol{k}=0}$ denotes a Hessian matrix, which can be readily diagonalized,

$$\begin{bmatrix} M_{x'x'} & M_{x'y'} \\ M_{y'x'} & M_{y'y'} \end{bmatrix} = \begin{bmatrix} S_{xx'} & S_{yx'} \\ S_{xy'} & S_{yy'} \end{bmatrix} \begin{bmatrix} m_x & 0 \\ 0 & m_y \end{bmatrix} \begin{bmatrix} S_{xx'} & S_{xy'} \\ S_{yx'} & S_{yy'} \end{bmatrix}. \tag{S88}$$

where $S_{ij'}$ is a unitary matrix, and ultimately yields the result,

$$\omega_{exc,\boldsymbol{k}} \approx \bar{\omega}'_{eff} + m_x k_x^2 + m_y k_y^2 \tag{S89a}$$

$$\approx \bar{\omega}_{eff} + 2J_x \cos k_x \Delta_x + 2J_y \cos k_y \Delta_y, \tag{S89b}$$

where $k_i = S_{ix'} k_{x'} + S_{iy'} k_{y'}$, and for our simulation, we choose (arbitrary) effective unit cell dimensions Δ_i such that $J_i = -\frac{m_i}{\Delta_i^2}$ for $i = x, y$, and $\bar{\omega}'_{eff} = \bar{\omega}_{eff} + 2J_x + 2J_y$; this identification renders Eqs. (S89a) and (S89b) equal up to quadratic order in k_i. We have thus arrived at a very convenient expression; Eq. (S89b) shows that the oblique lattice renders the same long-wavelength physics as a much simpler rectangular lattice with only NN interactions. This approximation is insightful in that it exposes the physical origin of the global gap; it also remains valid for our purposes as the topological phenomena of our interest occurs at small k_i.

For a fixed value of Δ_h, we Monte Carlo sample through the parameters $r \equiv \frac{\Delta_v}{\Delta_h} \in [0,2]$, $\alpha \in [0,\pi]$, and $\beta \in [0,\pi]$ and record those which yield $m_x, m_y < 0$. We observe that only ~8% of the parameter space satisfies the H-aggregate condition we are looking for. One such set of parameters is $\alpha' = 1.19 (\sim 68.5\,\text{degrees})$, $\beta = 0.23 (\sim 13.1\,\text{degrees})$, $r = 1.2$, yielding $(m_x, m_y) = -(1.49, 0.44) J_0 \Delta_h^2$, where $J_0 \equiv \frac{\eta \mu^2}{\Delta_h^3}$ sets the energy scale of the dipolar interactions. The associated eigenvector matrix is,

$$\begin{bmatrix} S_{xx'} & S_{yx'} \\ S_{xy'} & S_{yy'} \end{bmatrix} = \begin{bmatrix} -0.91 & -0.41 \\ 0.41 & -0.91 \end{bmatrix} = \begin{bmatrix} \cos\theta & -\sin\theta \\ \sin\theta & \cos\theta \end{bmatrix} \tag{S90}$$

where we obtain $\theta = 2.72(\sim 155.7^o)$, which defines the angle of rotation of our temporary coordinates $x'y'$ with respect to the original ones xy; then, $\alpha = \alpha' + \theta = 3.9(\sim 223^o)$. Now, each nanopillar has a collective transition dipole moment value of $\mu_0 = \sqrt{N_{np}}|\boldsymbol{p_n}| = \sqrt{N_{np}} \times 10\,\mathrm{D} = \sqrt{W_x W_y W_z \rho_{np}} \times 10\,\mathrm{D}$. Choosing the nanopillars to be separated from one another by Δ_h, we get a value for the energy scale of $J_0 = \frac{\eta W_x W_y W_z \rho_{np}}{\Delta_h^3} \times 100\,\mathrm{D}^2$. Taking $\rho_{np} = 37\,\mathrm{molecules/nm}^3$, we obtain,

$$J_x = -\frac{m_x}{\Delta_x^2} = 3.45 \times 10^3\ \mathrm{meV} \times \zeta_x$$
$$J_y = -\frac{m_y}{\Delta_y^2} = 1.02 \times 10^3\ \mathrm{meV} \times \zeta_y$$

where $\zeta_i = \frac{W_x W_y W_z}{\Delta_h \Delta_i^2}$ are dimensionless ratios which govern the effective dispersion of the superlattice. By choosing the physically reasonable parameters $\Delta_h = 100\,\mathrm{nm}$, $W_x = 7.5\,\mathrm{nm}$, $W_y = 50\,\mathrm{nm}$, $W_z = 70\,\mathrm{nm}$, and $\bar{\omega}'_{eff} = 2.15\,\mathrm{eV}$ as well as the effective simulation parameters $\Delta_x = \Delta_y = 50\,\mathrm{nm}$, we obtain $\Delta_v = r\Delta_h = 88\,\mathrm{nm}$, $\zeta_x = \zeta_y = 0.105$, $J_x = 362\,\mathrm{meV}$, $J_y = 107\,\mathrm{meV}$, and $\bar{\omega}_{eff} = 3.09\,\mathrm{eV}$. We emphasize that J_x and J_y can have arbitrary values which depend on our choice of parameters Δ_x and Δ_y. The latter set the spatial resolution of our real space simulations, and hence, the size of the systems we can computationally study. These simulations are carried out in order to calculate edge states as well as understand the effects of disorder.

We note that when choosing parameters, we need to make sure that (a) the nanopillars do not yuxtapose each other and (b) the number of chromophores in the organic layer is large enough to achieve considerable coupling with the SPs (see Eqs. (S96) and (S99)). Condition (a) is easily checked computationally and graphically. With respect to condition (b), we note that the surface area of the $ABCD$ parallelogram in Fig. S5 is $\Delta_h \Delta_y \sin\beta$. It contains two nanopillars of surface area $W_x W_y$. The surface coverage fraction of the organic layer is hence,

$$f = \frac{2W_x W_y}{\Delta_h \Delta_v \sin\beta}. \tag{S91}$$

For our chosen parameters, $f = 0.38$. In general, we need both f and W_z to not be very small ($f >\sim 0.2$, $W_z >\sim 40\,\mathrm{nm}$).

In the next subsections, we shall work with the effective rectangular superlattice of $N_x \times N_y$ nanopillars (where N_i is the number of nanopillars along the i-th direction) instead of the original monoclinic one. This is a good approximation not only for the interactions between the various nanopillars, but also for the exciton-SP couplings, as long we use the average density of the original monoclinic lattice (see Eqs. (S96) and (S99)).

B. Exciton-SP couplings

We are now ready to discuss the effective interaction between SPs and a single nanopillar. Consider the dipole operator $\hat{\boldsymbol{p}}_{\boldsymbol{m}s} = \boldsymbol{p}_{\boldsymbol{m}s}(b^\dagger_{\boldsymbol{m}s} + b_{\boldsymbol{m}s})$, where $b^\dagger_{\boldsymbol{m}s}(b_{\boldsymbol{m}s})$ creates (annhilates) an exciton at the $\boldsymbol{m}s$-th chromophore of some nanopillar. The time-independent electric field operator is $\hat{\vec{\mathscr{E}}}'(\boldsymbol{r}) \equiv \sum_{\boldsymbol{k}} \sqrt{\frac{\omega(\boldsymbol{k})}{2\epsilon_0 S L_{\boldsymbol{k}}}} a_{\boldsymbol{k}} \vec{E}'(\boldsymbol{k}) + \mathrm{h.c.}$, which results from transforming Eq. (S55a) from the Heisenberg to the Schrodinger picture by removing the dynamical phases $e^{-i\omega(\boldsymbol{k})t}$ (see Eqs. (S18a) and (S20a)), i.e., $\vec{E}'(\boldsymbol{k}) \equiv \vec{E}(\boldsymbol{k}) e^{i\omega(\boldsymbol{k})t}$. Using Eq. (S74) and (S75), the dipolar coupling between the $\boldsymbol{n}$th nanopillar and the SP modes is given by

$$\begin{aligned} H^{(\boldsymbol{n})}_{exc-SP} &= -\sum_{\boldsymbol{m},s} \hat{\boldsymbol{p}}_{\boldsymbol{m}s} \cdot \hat{\vec{\mathscr{E}}}'(\boldsymbol{r}) \\ &= \sum_{\boldsymbol{k},\boldsymbol{m},s} \mathscr{J}_{\boldsymbol{k},\boldsymbol{m}s} a_{\boldsymbol{k}} b^\dagger_{\boldsymbol{m}s} e^{i\boldsymbol{k}\cdot\boldsymbol{r}_{\boldsymbol{m}}} + \mathrm{h.c.}, \end{aligned} \tag{S92}$$

where the sum over $\boldsymbol{m}s$ is restricted to the chromophores in the $\boldsymbol{n}$-th nanopillar. We have also used the rotating-wave approximation to discard far-off-resonant terms of the form $a_{\boldsymbol{k}}\sigma_{\boldsymbol{n}s}$ and $a^\dagger_{\boldsymbol{k}}\sigma^\dagger_{\boldsymbol{n}s}$. Using Eq. (S55a), the corresponding coupling is given by,

$$\mathscr{J}_{\boldsymbol{k},\boldsymbol{ms}} = -\sqrt{\frac{\omega(\boldsymbol{k})}{2\epsilon_0 S L_{\boldsymbol{k}}}}\, e^{-\alpha(\boldsymbol{k}) z_s}\, \boldsymbol{p}_{\boldsymbol{ms}} \cdot \boldsymbol{E}(\boldsymbol{k}, z_s), \tag{S93}$$

where, depending on whether we use the two-layer or three-layer setup results, we make the following substitutions,

	For two-layer setup	
$L_{\boldsymbol{k}}$	$L_{\boldsymbol{k}0}$	Eq. (S50)
α	α_{d0}	Eq. (S24b)
$\boldsymbol{E}(\boldsymbol{k}, z_s)$	$\boldsymbol{E}_{MO}(\boldsymbol{k}, z_s) = \boldsymbol{E}_{d0}(\boldsymbol{k}) + g\boldsymbol{E}_{d1}(\boldsymbol{k}, z_s)$	Eqs. (S40a), (S41a)

	For three-layer setup	
$L_{\boldsymbol{k}}$	$L_{\boldsymbol{k}0}$	Eq. (S78)
α	α_{org0}	Eq. (S66b)
$\boldsymbol{E}(\boldsymbol{k}, z_s)$	$\boldsymbol{E}_{org}(\boldsymbol{k}, z_s) = \boldsymbol{E}_{org0}(\boldsymbol{k}) + g\boldsymbol{E}_{org1}(\boldsymbol{k}, z_s)$	Eqs. (S72a), (S73a), (S73b), (S76).

Eq. (S93) exposes the 3D nature of our problem with its z_s dependence: there is an exponential contribution $e^{-\alpha(\boldsymbol{k}) z_s}$ from the SP evanescent field, and even a linear correction in z_s due to $\boldsymbol{E}_{d1}$ for the two-layer setup. In any case, it will prove convenient to derive an effective 2D description for our model. We have two ways to do so.

1. *Mean-field approximation (MFA)*

Using Eqs. (S92) and (S93),

$$H^{(\boldsymbol{n})}_{exc-SP} = -\sum_{\boldsymbol{k}} \sqrt{\frac{\omega(\boldsymbol{k})}{2\epsilon_0 S L_{\boldsymbol{k}}}}\, e^{-\alpha(\boldsymbol{k})\bar{z}(\boldsymbol{k})}\, a_{\boldsymbol{k}} \boldsymbol{p}_{\boldsymbol{ms}} \cdot \left[\sum_{\boldsymbol{ms}} \boldsymbol{E}(\boldsymbol{k}, z_s) e^{i\boldsymbol{k}\cdot(\boldsymbol{r}_{\boldsymbol{m}} - \boldsymbol{r}_{\boldsymbol{n}}) - \alpha_0(\boldsymbol{k})(z_s - \bar{z}(\boldsymbol{k}))}\, b^\dagger_{\boldsymbol{ms}} \right] e^{i\boldsymbol{k}\cdot\boldsymbol{r}_{\boldsymbol{n}}} + \text{c.c.} \tag{S94a}$$

$$\approx -\sum_{\boldsymbol{k}} \sqrt{\frac{\omega(\boldsymbol{k})}{2\epsilon_0 S L_{\boldsymbol{k}}}}\, e^{-\alpha(\boldsymbol{k})\bar{z}(\boldsymbol{k})}\, \boldsymbol{E}(\boldsymbol{k}, \bar{z}(\boldsymbol{k})) \cdot \boldsymbol{\mu}_{\boldsymbol{n}} a_{\boldsymbol{k}} \sigma^\dagger_{\boldsymbol{n}} e^{i\boldsymbol{k}\cdot\boldsymbol{r}_{\boldsymbol{n}}} + \text{c.c.}, \tag{S94b}$$

where we have formally taken $\bar{z}(\boldsymbol{k})$ to be an average ($\boldsymbol{k}$-dependent) vertical position for the chromophores in the nanopillar (we will discuss how to compute this parameter later, see Eq. (S101)), made the MFA that $e^{i\boldsymbol{k}\cdot(\boldsymbol{r}_{\boldsymbol{m}} - \bar{\boldsymbol{r}}) - \alpha_0(\boldsymbol{k})(z_s - \bar{z})} \approx 1$, assumed that the dipoles $\boldsymbol{p}_{\boldsymbol{ms}} = \boldsymbol{p}_{\boldsymbol{n}}$ for all the chromophores in the $\boldsymbol{n}$-th nanopillar, and defined the collective exciton operator,

$$\sigma^\dagger_{\boldsymbol{n}} = \frac{1}{\sqrt{N_{np}}} \sum_{\boldsymbol{ms}} b^\dagger_{\boldsymbol{ms}}, \tag{S95}$$

such that its corresponding transition dipole is superradiantly enhanced at $\boldsymbol{\mu}_{\boldsymbol{n}} = \sqrt{N_{np}}\boldsymbol{p}_{\boldsymbol{n}}$.

Having addressed the effective interaction between a single nanopillar and the SP modes, we can move on to the description of the superlattice, $H_{exc-SP} = \sum_{\boldsymbol{n}} H^{(\boldsymbol{n})}_{exc-SP}$. If $\boldsymbol{\mu}_{\boldsymbol{n}} = \boldsymbol{\mu}$ and we assume periodic boundary conditions (PBCs), we can construct Fourier $\boldsymbol{k}$ modes for the excitons too, $\sigma^\dagger_{\boldsymbol{k}} = \frac{1}{\sqrt{N_x N_y}} \sum_{\boldsymbol{n}} \sigma^\dagger_{\boldsymbol{n}} e^{i\boldsymbol{k}\cdot\boldsymbol{r}_{\boldsymbol{n}}}$. Then, we arrive at the Hamiltonian, $H_{exc-SP} = \sum_{\boldsymbol{k}} H_{exc-SP,\boldsymbol{k}} = \sum_{\boldsymbol{k}} \mathscr{J}(\boldsymbol{k}) a_{\boldsymbol{k}} \sigma^\dagger_{\boldsymbol{k}} + \text{h.c.}$, where

$$\mathscr{J}(\boldsymbol{k}) = \sqrt{\left(\frac{N_x N_y}{S}\right)\left(\frac{\omega(\boldsymbol{k})}{2\epsilon_0 L_{\boldsymbol{k}0}}\right)}\, e^{-\alpha_0(\boldsymbol{k})\bar{z}(\boldsymbol{k})}\, \boldsymbol{\mu} \cdot \boldsymbol{E}(\boldsymbol{k}), \tag{S96}$$

and $\boldsymbol{k}$ runs for all the allowed discretized wavevectors $k_i = -\frac{\pi}{\Delta_i} + \frac{2\pi}{N_i \Delta_i} q_i$ for $q_i = 0, 1, \cdots, N_i - 1$.

Within the MFA, we have achieved to represent each nanopillar as a single collective transition dipole $\boldsymbol{\mu}_{\boldsymbol{n}}$ associated with the operator $\sigma^\dagger_{\boldsymbol{n}}$. There is, however, an ambiguity in this approximation, namely, the criterion to optimize the parameter $\bar{z}(\boldsymbol{k})$. We will discuss this in Subsec. (III B 3).

2. Beyond the MFA

Going back to Eq. (S94a) and assuming $\boldsymbol{p}_{\boldsymbol{ms}} = \boldsymbol{p}_{\boldsymbol{n}}$, we can consider alternative nanopillar modes. We follow González-Tudela, *et al* [10]. Let us define the new modes (distinguished from the others by the overbar notation),

$$\bar{\sigma}^{\dagger}_{\boldsymbol{n}}(\boldsymbol{k}) = \frac{1}{\sqrt{\mathcal{N}}}\sum_{\boldsymbol{ms}} \boldsymbol{p}_{\boldsymbol{n}} \cdot \boldsymbol{E}(\boldsymbol{k}, z_s) e^{i\boldsymbol{k}\cdot(\boldsymbol{r}_{\boldsymbol{m}}-\boldsymbol{r}_{\boldsymbol{n}})-\alpha_0(\boldsymbol{k})z_s} b^{\dagger}_{\boldsymbol{ms}}, \tag{S97}$$

where the corresponding normalization is given by,

$$\begin{aligned}\mathcal{N} &= \sum_{\boldsymbol{ms}} \left| \boldsymbol{p}_{\boldsymbol{n}} \cdot \boldsymbol{E}(\boldsymbol{k}, z_s) e^{i\boldsymbol{k}\cdot(\boldsymbol{r}_{\boldsymbol{m}}-\boldsymbol{r}_{\boldsymbol{n}})-\alpha_0(\boldsymbol{k})z_s} \right|^2 \\ &\approx \frac{N_{np}}{W_z}\int_{z_0}^{z_f} dz |\boldsymbol{p}_{\boldsymbol{n}} \cdot \boldsymbol{E}(\boldsymbol{k}, z)|^2 e^{-2\Re\alpha_0(\boldsymbol{k})z}.\end{aligned} \tag{S98}$$

where we identified $z_f - z_0 = W_z$ as the vertical thickness of each nanopillar. Introducing the corresponding $\boldsymbol{k}$ mode $\bar{\sigma}^{\dagger}_{\boldsymbol{k}} = \frac{1}{\sqrt{N_x N_y}}\sum_{\boldsymbol{n}} \bar{\sigma}^{\dagger}_{\boldsymbol{n}}(\boldsymbol{k}) e^{i\boldsymbol{k}\cdot\boldsymbol{r}}$, Eq. (S94a) becomes $H_{exc-SP} = \sum_{\boldsymbol{k}} H_{exc-SP,\boldsymbol{k}} \approx \sum_{\boldsymbol{k}} \bar{\mathscr{J}}(\boldsymbol{k}) a_{\boldsymbol{k}} \bar{\sigma}^{\dagger}_{\boldsymbol{k}} + \text{h.c.}$, where,

$$\bar{\mathscr{J}}(\boldsymbol{k}) \approx \sqrt{\rho\left(\frac{\omega(\boldsymbol{k})}{2\epsilon_0 L_{\boldsymbol{k}0}}\right)} \sqrt{\int_{z_0}^{z_f} dz e^{-2\Re\alpha_0(\boldsymbol{k})z} |\boldsymbol{p}_{\boldsymbol{n}} \cdot \boldsymbol{E}(\boldsymbol{k}, z)|^2}, \tag{S99}$$

where we have identified

$$\rho = \frac{N_x N_y N_{np}}{S W_z} = \underbrace{\frac{(N_x W_x)(N_y W_y)}{S}}_{<1} \rho_{np} \tag{S100}$$

as the *average* density of chromophores in the organic superlattice which, due to the "void space" between nanopillars, is lower than ρ_{np}. Except for a different convention in the phases of our exciton modes $\bar{\sigma}^{\dagger}_{\boldsymbol{k}}$, this solution has the same structure as the one presented in [10], even though the latter deals with an organic layer of uniform density.

3. Comparison

When we wrote $H_{exc-SP} \approx \sum_{\boldsymbol{k}} \mathscr{J}(\boldsymbol{k}) a_{\boldsymbol{k}} \sigma^{\dagger}_{\boldsymbol{k}} + \text{h.c.}$, we made a MFA to Eq. (S94a) by invoking definitions for the mode $\sigma^{\dagger}_{\boldsymbol{n}}$ and the coupling $\mathscr{J}(\boldsymbol{k})$ (Eqs. (S95) and (S96)). The essence of this approximation is the exponential factor $e^{-\alpha_0(\boldsymbol{k})\bar{z}(\boldsymbol{k})}$ in $\mathscr{J}(\boldsymbol{k})$, which implies that when each nanopillar interacts with the $\boldsymbol{k}$-th electromagnetic mode, it behaves as a collective dipole placed at the effective height $z = \bar{z}(\boldsymbol{k})$. On the other hand, when going beyond the MFA, we introduced $\bar{\sigma}^{\dagger}_{\boldsymbol{n}}(\boldsymbol{k})$ and $\bar{\mathscr{J}}(\boldsymbol{k})$ (Eqs. (S97) and (S99)) and showed that $H_{exc-SP} \approx \sum_{\boldsymbol{k}} \bar{\mathscr{J}}(\boldsymbol{k}) a_{\boldsymbol{k}} \bar{\sigma}^{\dagger}_{\boldsymbol{k}} + \text{h.c.}$ is an exact representation of Eq. (S94a) (notwithstanding the excellent approximations of converting the sums over chromophores to integrals and the PBCs). Hence, $\bar{\sigma}^{\dagger}_{\boldsymbol{k}}$ (and not $\sigma^{\dagger}_{\boldsymbol{k}}$) is the natural exciton mode which couples to the SP mode $a^{\dagger}_{\boldsymbol{k}}$.

The solution beyond MFA might be a more convenient description if one is interested in a careful description of the energetics of the problem. However, for purposes of the topological characterization of the plexciton bandstructure, it is more pertinent to adopt the MFA description. Notice from Eq. (S97) that $\bar{\sigma}^{\dagger}_{\boldsymbol{n}}(\boldsymbol{k})$ depends explicitly on $\boldsymbol{k}$, so that the Fourier modes $\bar{\sigma}^{\dagger}_{\boldsymbol{k}} = \frac{1}{\sqrt{N_x N_y}}\sum_{\boldsymbol{n}} \bar{\sigma}^{\dagger}_{\boldsymbol{n}}(\boldsymbol{k}) e^{i\boldsymbol{k}\cdot\boldsymbol{r}}$ have an additional dependence on $\boldsymbol{k}$ beyond the phase factor $e^{i\boldsymbol{k}\cdot\boldsymbol{r}}$. This introduces a technicality for the numerical computation of the Chern number for each plexciton band, which we wish to avoid at present. This complication does not occur in the MFA, where $\sigma^{\dagger}_{\boldsymbol{n}}$ uniformly sums over the excitons operators $b^{\dagger}_{\boldsymbol{ms}}$ for a given nanopillar regardless of $\boldsymbol{k}$. Thus, we make a compromise: we formally use the structure of the MFA, but heuristically make the energetic approximation $\left|\mathscr{J}(\boldsymbol{k})\right| = \bar{\mathscr{J}}(\boldsymbol{k})$. Comparing Eqs. (S96) and (S99), this identity requires that $\bar{z}(\boldsymbol{k})$ satisfies,

$$\left| \boldsymbol{p}_{\boldsymbol{n}} \cdot \boldsymbol{E}(\boldsymbol{k}, \bar{z}(\boldsymbol{k})) e^{-\alpha_{org0}(\boldsymbol{k})\bar{z}(\boldsymbol{k})} \right| = \sqrt{\frac{1}{W_z}\int_{z_0}^{z_f} dz |\boldsymbol{p}_{\boldsymbol{n}} \cdot \boldsymbol{E}(\boldsymbol{k}, z)|^2 e^{-2\Re\alpha_{org0}(\boldsymbol{k})z}}. \tag{S101}$$

This constraint has the appealing physical content of computing the mean-field effective position $\bar{z}(\boldsymbol{k})$ of the collective nanopillar dipole by averaging interaction of the SP with respect to the interval $z \in [z_i, z_f]$. Operationally, however, it is not necessarily to solve for $\bar{z}(\boldsymbol{k})$, as having the value of $\bar{\mathscr{J}}(\boldsymbol{k})$ in Eq. (S99) suffices for our calculations.

To remind ourselves, when dealing with the dispersion of the organic layer alone, we have coarse grained it into an effective rectangular superlattice. However, when computing the exciton-SP coupling via Eq. (S99), ρ must be taken to be the density of the original monoclinic superlattice. Eq. (S100) is undetermined as N_x and N_y are artificial simulation parameters, instead, we shall write

$$\rho = f\rho_{np}, \tag{S102}$$

the average density is equal to the surface coverage fraction times the original nanopillar density.

4. *Representative coupling values*

Figs. S6 and S7 plot representative exciton-SP coupling values $\bar{\mathscr{J}}(\boldsymbol{k})$ using Eq. (S99) for the two-layer and three-layer setups, respectively. We display calculations for different orientations of the transition dipoles of the nanopillars, when $\boldsymbol{\mu} \parallel \hat{\boldsymbol{k}}$, $\boldsymbol{\mu} \parallel \hat{\boldsymbol{\theta}}_{\boldsymbol{k}}$, and $\boldsymbol{\mu} \parallel \hat{\boldsymbol{z}}$. Throughout the plots, we have chosen silver Drude parameters $\epsilon_\infty \sim 4$, $\omega_P \sim 9$ eV and $g = 0.3$. Each of the panels displays results corresponding to a particular dielectric permittivity ϵ_d and the base height of the nanopillars z_0, and fixing the same organic layer height $W_z = 70\,\text{nm}$. Taking the parameters for the organic superlattice described in Subsec. and assuming $\rho_{np} = 37\,\text{chromophores/nm}^3$, the average density using Eq. (S102) is $\rho = 14\,\text{chromophores/nm}^3$. Fig. S6 corresponds to the physical scenario where the organic nanopillars are "embedded" in the MO dielectric layer starting at the base height z_0, while Fig. S7 assumes that the MO dielectric layer has a width a and the base height of the nanopillars is also at a.

As a reminder, in the absence of the MO effect, the electric field of the $\boldsymbol{k}$-th SP mode has no tangential component (see Eqs. (S40a), (S72a)). Thus, the blue curves in the plots ($\boldsymbol{\mu} \parallel \hat{\boldsymbol{\theta}}$) must vanish identically for $g = 0$. For $g \neq 0$, these couplings scale linearly with g (see Eqs. S41a, S76), so it is easy to predict these perturbative exciton-SP couplings for other values of g. On the other hand, the red ($\boldsymbol{\mu} \parallel \hat{\boldsymbol{k}}$) and black ($\boldsymbol{\mu} \parallel \hat{\boldsymbol{z}}$) curves are independent of the value of g, as they are $O(g^0)$. Notice that all the curves peak at some short wavevector k_{max}. The effective site energy $\bar{\omega}_{eff}$ (see Eq. (S87)) was optimized so that the exciton dispersion $H_{exc,\boldsymbol{k}}$ and the SP dispersion $H_{SP,\boldsymbol{k}}$ become degenerate (Dirac points) at wavevectors $\boldsymbol{k}^*$ satisfying $|\boldsymbol{k}^*| = k_{max}$. This is carried out so that upon inclusion of the MO effect, the topological anticrossing generated at the Dirac point $\boldsymbol{k}^*$ becomes as large as possible. The latter implies that one should maximize $\bar{\mathscr{J}}(\boldsymbol{k}^*)$ for $\boldsymbol{\mu} \parallel \hat{\boldsymbol{\theta}}_{\boldsymbol{k}}$.

The simulations displayed in the main text correspond to the first (upper left corner) panel of Fig. S6, where, yielding $\bar{\mathscr{J}}(\boldsymbol{k}^*) = 0.24\,\text{eV}$ for $\boldsymbol{\mu} \parallel \hat{\boldsymbol{\theta}}$, or equivalently, a topological anticrossing gap of $2\bar{\mathscr{J}}(\boldsymbol{k}^*) = 0.48\,\text{eV}$. This value becomes reasonably large compared to the linewidths of the exciton and SP modes even if we reduce g by a factor of three or four. Note that quite often, the largest couplings occur when $\boldsymbol{\mu} \parallel \hat{\boldsymbol{z}}$, reaching values which are comparable to the exciton site energies. This regime, known as ultra-strong coupling [20], is interesting in its own right and gives rise to novel effects, which are beyond the scope of our work. Unfortunately, for our purposes, we cannot exploit these large couplings, as they do not vanish for any $\boldsymbol{k}$ and hence, does not yield Dirac points (see main text).

A few interesting trends can be obtained from scanning through ϵ_d and z_0; some of these results are displayed in Figs. S6 and S7. First, couplings decrease as z_0 increases. This is not surprising, as owing to the evanescent nature of the SP fields, the coupling should be strongest for the chromophores that are closest to the interface at $z = 0$. Second, couplings decrease as the dielectric ϵ_d increases. Finally, notice that the three-layer setup yields very weak values of $\bar{\mathscr{J}}(\boldsymbol{k}^*)$ for $\boldsymbol{\mu} \parallel \hat{\boldsymbol{\theta}}_{\boldsymbol{k}}$. We believe that these two problems are related to index mismatch between the various interfaces. As mentioned in the main text, one possibility to ameliorate this problem is to embed the MO material inside of a low dielectric polymer.

An alternative solution to increase $\bar{\mathscr{J}}(\boldsymbol{k}^*)$ for $\boldsymbol{\mu} \parallel \hat{\boldsymbol{\theta}}_{\boldsymbol{k}}$ is to use materials with large g values at the UV/visible, which is what we need (recall the crossing between the SP and exciton dispersions at $\boldsymbol{k}^*$ happens at 3.1 eV in our calculation). Some examples of the latter are Co alloy films [21], orthoferrites [22], or spinels [23]. A caveat about the latter is that they are also highly absorptive at those same wavelengths (large imaginary part of ϵ_d, which we have neglected in this work). Ce substituted YIG has less of a problem in that regard [24]. We are currently addressing all these possibilities, including different stacking geometries, in order to induce strong MO effects.

[1] V. Kuzmiak, S. Eyderman, and M. Vanwolleghem. Controlling surface plasmon polaritons by a static and/or time-dependent external magnetic field. *Phys. Rev. B*, 86:045403, 2012.

[2] M.C. Onbasli, T. Goto, X. Sun, N. Huynh, and C. A. Ross. Integration of bulk-quality thin film magneto-optical cerium-doped yttrium iron garnet on silicon nitride photonic substrates. *Opt. Express*, 22(21):25183–25192, 2014.

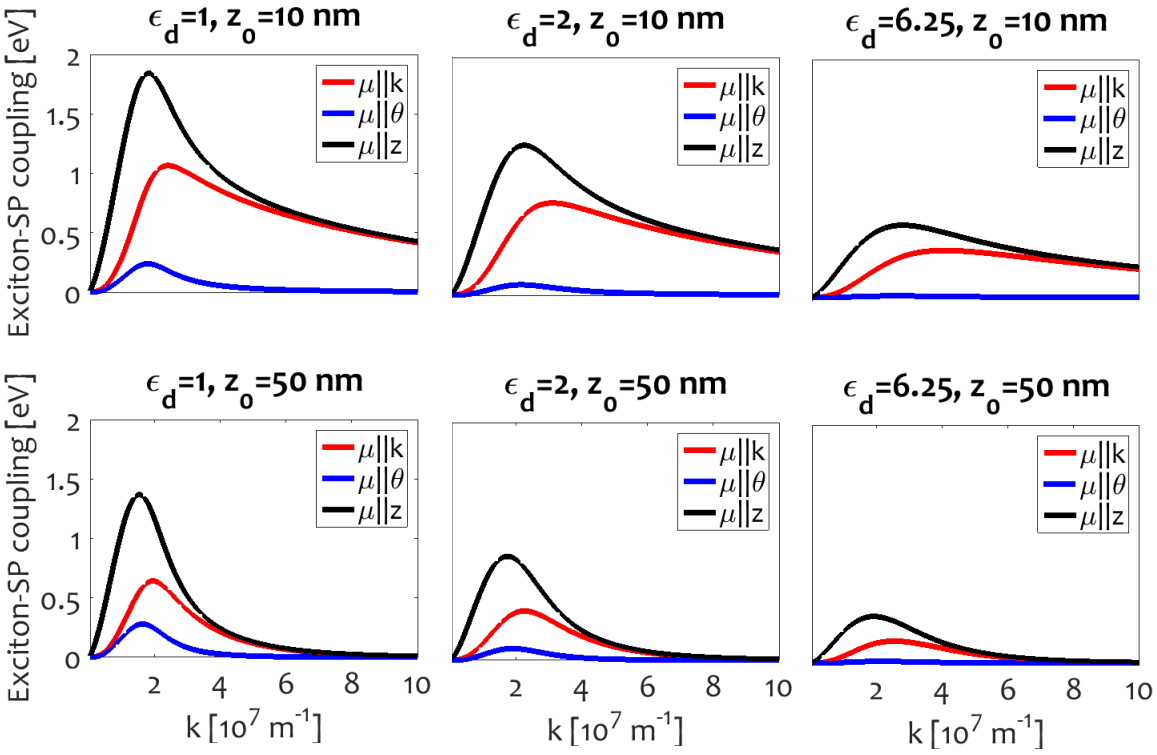

Figure S6. *Representative exciton-SP coupling values for two-layer (metal-MO dielectric) setup.* The calculations have been carried out using Eq. (S99). We display results for different orientations of the transition dipoles of the nanopillars, when $\boldsymbol{\mu} \parallel \hat{\boldsymbol{k}}$, $\boldsymbol{\mu} \parallel \hat{\boldsymbol{\theta}}$, and $\boldsymbol{\mu} \parallel \hat{\boldsymbol{z}}$. Notice that all the curves have maxima at short wavevectors. The calculations assume that $\epsilon_\infty \sim 4$, $\omega_P \sim 9$ eV, $g = 0.3$, and the height of the nanopillars being $W_z = 70$ nm.

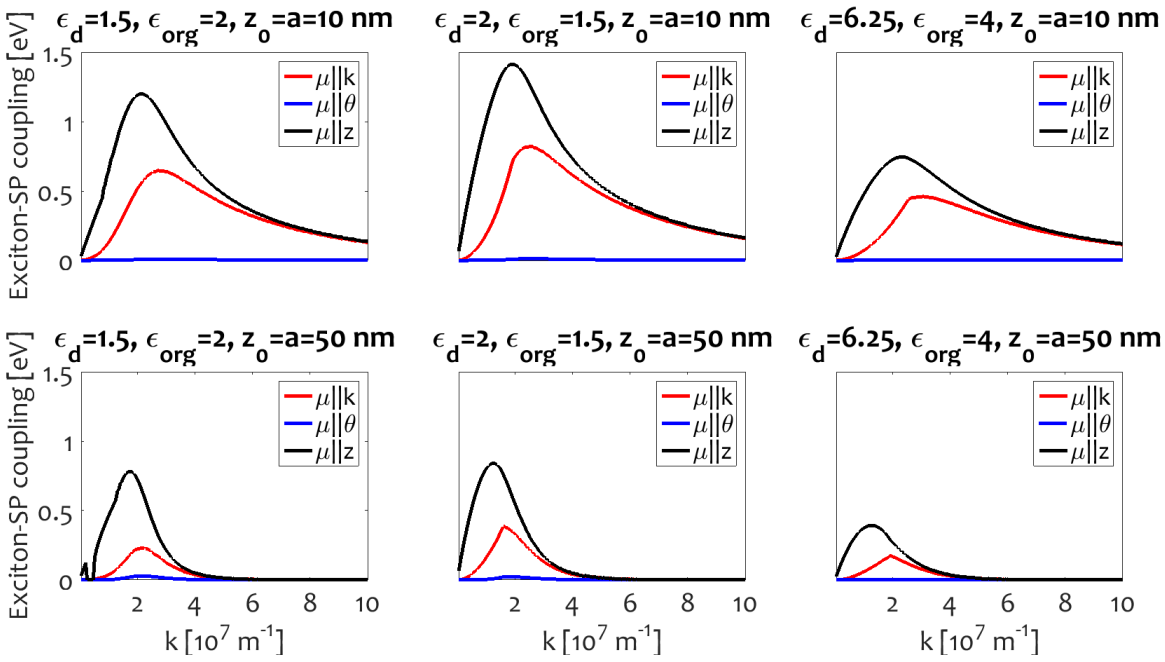

Figure S7. *Representative exciton-SP coupling values for three-layer (metal-MO dielectric-organic) setup.* Just as with Fig. S6, the calculations have been carried out using Eq. (S99). We display results for different orientations of the transition dipoles of the nanopillars, when $\boldsymbol{\mu} \parallel \hat{\boldsymbol{k}}$, $\boldsymbol{\mu} \parallel \hat{\boldsymbol{\theta}}$, and $\boldsymbol{\mu} \parallel \hat{\boldsymbol{z}}$. Notice that all the curves have maxima at short wavevectors. The calculations assume that $\epsilon_\infty \sim 4$, $\omega_P \sim 9$ eV, $g = 0.3$, and the height of the nanopillars being $W_z = 70$ nm.

[3] G. F Dionne. *Magnetic oxides*. Springer, 2009.

[4] P.R. West, S. Ishii, G.V. Naik, N.K. Emani, V.M. Shalaev, and A. Boltasseva. Searching for better plasmonic materials. *Laser Photon. Rev.*, 4(6):795–808, 2010.

[5] J. Bellessa, C. Bonnand, J. C. Plenet, and J. Mugnier. Strong coupling between surface plasmons and excitons in an organic semiconductor. *Phys. Rev. Lett.*, 93:036404, 2004.

[6] A. O. Govorov, G. W. Bryant, W. Zhang, T. Skeini, J. Lee, N. A. Kotov, J. M. Slocik, and R. R. Naik. Exciton-plasmon interaction and hybrid excitons in semiconductor-metal nanoparticle assemblies. *Nano Lett.*, 6(5):984–994, 2006.

[7] Y. Sugawara, T. A. Kelf, J. J. Baumberg, M. E Abdelsalam, and P. N. Bartlett. Strong coupling between localized plasmons and organic excitons in metal nanovoids. *Phys. Rev. Lett.*, 97:266808, 2006.

[8] D. E. Chang, A. S. Sørensen, P. R. Hemmer, and M. D. Lukin. Strong coupling of single emitters to surface plasmons. *Phys. Rev. B*, 76:035420, 2007.

[9] Adi Salomon, Robert J. Gordon, Yehiam Prior, Tamar Seideman, and Maxim Sukharev. Strong coupling between molecular excited states and surface plasmon modes of a slit array in a thin metal film. *Phys. Rev. Lett.*, 109:073002, 2012.

[10] A. González-Tudela, P. A. Huidobro, L. Martín-Moreno, C. Tejedor, and F. J. García-Vidal. Theory of strong coupling between quantum emitters and propagating surface plasmons. *Phys. Rev. Lett.*, 110:126801, 2013.

[11] P. Törmä and W.L. Barnes. Strong coupling between surface plasmon polaritons and emitters: a review. *Rep. Prog. Phys.*, 78(1):013901, 2015.

[12] H. Fan, H. R Bentley, K. R Kathan, P. Clem, Y. Lu, and C. J. Brinker. Self-assembled aerogel-like low dielectric constant films. *J. Non-Cryst. Solids*, 285(1):79–83, 2001.

[13] K.W. Chiu and J.J. Quinn. Magneto-plasma surface waves in solids. *Nuovo Cimento B*, 10(1):1–20, 1972.

[14] S. A. Maier. *Plasmonics: Fundamentals and Applications*. Springer, 2007.

[15] L. Novotny and B. Hecht. *Principles of Nano-Optics*. Cambridge University Press, 2012.

[16] A. Archambault, F. Marquier, J.-J. Greffet, and C. Arnold. Quantum theory of spontaneous and stimulated emission of surface plasmons. *Phys. Rev. B*, 82:035411, 2010.

[17] H. DeVoe. Optical properties of molecular aggregates. i. classical model of electronic absorption and refraction. *J. Chem. Phys.*, 41(2):393–400, 1964.

[18] H. DeVoe. Optical properties of molecular aggregates. ii. classical theory of the refraction, absorption, and optical activity of solutions and crystals. *J. Chem. Phys.*, 43(9):3199–3208, 1965.

[19] S. Valleau, S. K. Saikin, D. Ansari-Oghol-Beig, M. Rostami, H. Mossallaei, and A. Aspuru-Guzik. Electromagnetic study of the chlorosome antenna complex of chlorobium tepidum. *ACS Nano*, 8(4):3884–3894, 2014.

[20] Y. Todorov, A. M. Andrews, R. Colombelli, S. De Liberato, C. Ciuti, P. Klang, G. Strasser, and C. Sirtori. Ultrastrong light-matter coupling regime with polariton dots. *Phys. Rev. Lett.*, 105:196402, 2010.

[21] V.V. Temnov, G. Armelles, U. Woggon, D. Guzatov, A. Cebollada, A. Garcia-Martin, J.M. Garcia-Martin, T. Thomay, A. Leitenstorfer, and R. Bratschitsch. Active magneto-plasmonics in hybrid metal–ferromagnet structures. *Nat. Photon.*, 4(2):107–111, 2010.

[22] F. J. Kahn, P. S. Pershan, and J. P. Remeika. Ultraviolet magneto-optical properties of single-crystal orthoferrites, garnets, and other ferric oxide compounds. *Phys. Rev.*, 186:891–918, 1969.

[23] W. F. J. Fontijn, P. J. Van der Zaag, L. F. Feiner, R. Metselaar, and M. A. C. Devillers. A consistent interpretation of the magneto-optical spectra of spinel type ferrites. *J. Appl. Phys.*, 85(8):5100, 1999.

[24] X. Y. Sun, Q. Du, T. Goto, M. C. Onbasli, D. H. Kim, N. M. Aimon, J. Hu, and C. A. Ross. Single-step deposition of cerium-substituted yttrium iron garnet for monolithic on-chip optical isolation. *ACS Photonics*, 2(7):856–863, 2015.